Investigation of a new mass matrix scheme with high-order numerical dissipation for the discretisation of three-dimensional turbulent flows

Rapport de stage Master 2

Sous la direction de M.Bruno KOOBUS
Mai-Juillet 2008
Institut de Mathématique et de Modélisation de Montpellier,
Université Montpellier II

Anca BELME

0.1 Remerciements

Je tiens a remercier avant tout M. Bruno KOOBUS, pour avoir accepter de diriger ses travaux, pour son enthousiasme pour la recherche, pour son soutien indéfectible qui m'a beaucoup aidé et motivé tout au long de cette année universitaire et pour m'avoir donne le goût de calcul scientifique.
Ma reconnaissance va également a M.Alain Dervieux pour m'avoir offert l'opportunité de pursuivre mon stage en une thèse de doctorat, pour l'intérêt qu'il a porté a mon travail et pour sa disponibilité bienveillante tout au long de mon stage.
Plus qu'une collègue, je tiens a remercier Mlle Hilde Ouvrard pour m'avoir aidé aussi bien dans le travail que dans toute autre chose dont j'ai eu besoin.
Je suis également reconnaissante a M.Michel Cuer et a M.Fabien Marche d'avoir bien voulu faire partie du jury, et a M.Patrick Redont et M.Baptiste Chapuisat pour leur support informatique.

Contents

Introduction

Turbulent flows have been and continue to be of great interest to the working engineer simply because most engeineering flows are indeed turbulent.

There are many opportunities to observe turbulent flows in our everyday surroundings, whether it be smoke from a cheminey, water in a river or waterfall, or the buffering of a strong wind.In observing a waterfall, we immediately see that the flow is unsteady, irregular, seemingly random and chaotic, and surely the motion of every eddy or droplet is unpredictable. In the plume formed by a solid racket motor, turbulent motions of many scales cand be observed, from eddies and bulges comparable in size to the width of the plume, to the smallest scales the camera can resolve. The features mentioned in these two exemples are common to all turbulent flows.

In enginneering applications turbulent flows are prevalent, but less easily seen. In the processing of liquids or gases with pumps, compressors, pipe lines, etc., the flows are generally turbulent.Similary the flows around vehicles,-e.g., airplanes, automobiles, ships and submarines are turbulent. The mixing of fuel and air in engines, boilers, and furnaces, and the mixing of the reactants in chemical reactors take place in turbulent flows.

In view of the importance of this subject, understanding turbulent flow is central to many important problems. So, it is natural that the study of turbulent flow has attracted wide-stread attention from scientists all over the world. However, progress has been limited and understanding turbulent flows remains a challenge. The main obstacles in turbulent are subjected to the features of turbulence, listed bellow :

- Turbulence is diffusive.
- Turbulence is not only chaotic motion and but also irregular motion.
- Turbulence is rotational and three dimensional.

- Turbulence is highly dissipative.
- Turbulence is a continuum phenomenon. The smallest scales of turbulence are mutch larger than the molecular scales in the enginnering application.
- Turbulence is associated with high levels of vorticity fluctuations. Small scales are generates by the vortex stretching mechanism.

Mathematically, as long as the continuum hypotesis is valid, turbulent flows are solutions to the Navier-Stokes equations of motion subjet to appropiate boundary conditions and initial conditions.

One of the pricipal challenges in studying turbulence is the unavailability of an analytic solution to the governing differential equations, except for a few very idealized flows.

Direct Numerical Simulation (DNS) of turbulent flows is feasible only for low Reynolds numbers (Re) due to the required computational resources, which already become prohibitively large for $Re \simeq 10^4$. For this reason, turbulence modeling is a necessary step for the numerical simulation of flows of engineering interest. In this context, the most widely used approach for the simulation of high-Reynolds number turbulent flows is the one based on the discretization of the Reynolds-Averaged Navier-Stokes equations (RANS). In the RANS approach, time averaging is applied to the Navier-Stokes equations and only the time-averaged flow is simulated. In this way a noticeable simplification of the problem is obtained, computational costs are drastically reduced and become almost independent of the Reynolds number when this is sufficiently large. However, RANS simulations usually have difficulties in providing accurate predictions for flows with massive separations, as for instance for the flow around bluff bodies. Indeed, RANS models are in general too dissipative to properly simulate the three-dimensional and unsteady phenomena occurring in such flows, yielding to significant discrepancies with respect to the experimental results.

An alternative approach is the Large-Eddy simulation (LES), in which a spatial filter is applied to the equations to get rid of small-scale turbulent fluctuations, which are thus modeled, while the remaining flow scales are directly simulated. In this way, the three-dimensionality and unsteadiness of the flow are naturally taken into account and the LES approach is generally more accurate, but also computationally more expensive, than the RANS one. Moreover, the cost of LES simulations increases as the flow Reynolds number is increased. Indeed, the grid has to be fine enough to resolve a significant part of the turbulent scales, and spatial resolution becomes particularly critical in the near-wall regions.

A recent approach to LES based on a Variational Multi-Scale (VMS) framework was intruced by Hughes et al. in Ref. [4]. The VMS-LES differs fundamentally from the traditional LES in a number of ways. In this approach, one does not filter the Navier-Stokes equations but uses instead a variational projection. This is an important difference because as performed in the traditional LES, filtering works well with periodic boundary conditions but raises mathematical issues in wall-bounded flows. The variational projection avoids these issues. Furthermore, the VMS-LES method separates the scales a priori-that is, before the simulation is started. And most importantly, it models the effect of the unresolved-scales only in the equations representing the smallest resolved-scales, and not in the equations for the large scales. Consequently, in the VMS-LES, energy is extracted from the fine resolved-scales by a subgrid scale (SGS) eddy-viscosity model, but no energy is directly extracted from the large structures in the flow.

The proposed model has been implemented in a numerical solver (AERO) for the Navier-Stokes equations in the case of compressible flows and perfect Newtonian gases, based on a mixed finite-element/finite-volume scheme formulated for unstructured grids made of tetrahedral elements. Finite elements (P1 type) and finite volumes are used to treat the diffusive and convective fluxes, respectively. Concerning the VMS approach, the version proposed in Ref. [5] for compressible flows and for the particular numerical method employed in AERO has been used

here.

The discretisation of the convective fluxes for the finite volume scheme used in the software AERO exhibits a lack of accuracy in the case of irregular mesh. In order to overcome this problem, we investigate on this work a new mass matrix scheme with high-order numerical dissipation for the discretization of turbulent flows.

The present report is organized as follows, we review in chapter 1 a mass matrix scheme for the 1D advection equation case and we analyse the stability of this scheme for explicit and implicit mode using Van Newmann analysis, chapter 2 contains the numerical method implemented in our CFD software, chapter 3 is consacreted to turbulence simulation. Results of the simulations and gaussian translation behavior are presented and discussed in sections 4.

Chapter 1

Mass Matrix Central Differencing scheme for the advection equation

1.1 Spatial 1D MUSCL formulation

Let us first consider the one-dimensional scalar conservation law

$$u_t + f(u)_x = 0 \tag{1.1}$$

We suppose $f \in C^1(R,R)$. We'll insist on particulary case where $f(u) = cu(c > 0)$.

Spatial discretisation

The finite-volume method is used for the discretization in space. Let x_j , $1 \leq j \leq N$ denote the discretization points of the mesh. For each discretization point, we state : $u_j \approx u(x_j)$ and we define the control cell C_j as the interval $[x_{j-\frac{1}{2}},x_{j+\frac{1}{2}}]$ where $x_{j+\frac{1}{2}} = \frac{x_j+x_{j+1}}{2}$.

We define the unknown vector $U = \{u_j\}$ as point approximation values of the function $u(x)$ in each node j of the mesh.
The time advancing scheme is written :

$$U_{j,t} + \Psi_j(U) = 0$$

where the vector $\Psi_j(U)$ is built according to approximations of $(f(u))_x$ defined at cell boundaries, as follows:

$$\Psi_j(U) = \frac{1}{\Delta x}(\Phi_{j+\frac{1}{2}} - \Phi_{j-\frac{1}{2}});\ \Phi_{j+\frac{1}{2}} = \Phi(u^-_{j+\frac{1}{2}}, u^+_{j+\frac{1}{2}}); \tag{1.2}$$

where $u^-_{j\pm\frac{1}{2}}$, $u^+_{j\pm\frac{1}{2}}$ are integration values of u at boundaries of control volume C_j and Φ is a numerical flux function defined here :

$$\Phi(u,v) = \frac{cu + cv}{2} - \frac{\delta}{2}c(v-u), \tag{1.3}$$

where the coefficient δ controls the spatial dissipation.
For the uppwind scheme(mode of a dissipation based on sixth order spatial derivatives) developped by Debiez et al., these reconstructed values are given by: $u^-_{j+\frac{1}{2}} = u_j + \frac{1}{2}\Delta u^-_{j+\frac{1}{2}}$ and $u^+_{j+\frac{1}{2}} = u_j - \frac{1}{2}\Delta u^+_{j+\frac{1}{2}}$ (same reconstruction for $u^-_{j-\frac{1}{2}}$ and $u^+_{j-\frac{1}{2}}$) where the slopes $\Delta u^-_{j+\frac{1}{2}}$ and $\Delta u^+_{j+\frac{1}{2}}$ are defined by:

$$\Delta u^-_{j+\frac{1}{2}} = (1-\beta)(u_{j-1} - u_j) + \beta(u_j - u_{j-1}) \tag{1.4}$$

$$+\theta^c(-u_{j-1} + 3u_j - 3u_{j+1} + u_{j+2}) \tag{1.5}$$

$$+\theta^d(-u_{j-2} + 3u_{j-1} - 3u_j + u_{j+1}) \tag{1.6}$$

and

$$\Delta u^{+}_{j+\frac{1}{2}} = (1-\beta)(u_{j+1}-u_j) + \beta(u_{j+2}-u_{j+1}) \tag{1.7}$$

$$+\theta^c(-u_{j-1}+3u_j-3u_{j+1}+u_{j+2}) \tag{1.8}$$

$$+\theta^d(-u_j+3u_{j+1}-3u_{j+2}+u_{j+3}) \tag{1.9}$$

We observe that for $\beta = \frac{1}{3}$,$\theta^c = \frac{-1}{10}$ and $\theta^d = \frac{-1}{15}$, this scheme becomes fifth-order accurate. The dissipation is then made of sixth-order derivatives and can be written as:

$$D_j(u) = \frac{D_{j+\frac{1}{2}}(u) - D_{j-\frac{1}{2}}(u)}{\Delta x}$$

where $D_{j+\frac{1}{2}}(u) = \frac{\delta c}{60}(-u_{j-2}+5u_{j-1}-10u_j+10u_{j+1}-5u_{j+2}+u_{j+3})$

1.2 Mass Matrix Scheme with central differencing

The usual central-differences three-point scheme is penalized by a dispersion leading error. This error is compensated in the case where we introduce the finite-element P_1 consistent mass matrix. The time advancing is written:

$$MU(t) + \Delta x \Psi(U) = 0 \tag{1.10}$$

$$(MU(t))_j = m_{j,j-1}U_{j-1,t} + m_{j,j}U_{j,t} + m_{j,j+1}U_{j+1,t}$$

where

$$\begin{aligned} m_{j,j-1} &= 1/6\Delta x \\ m_{j,j} &= 2/3\Delta x \\ m_{j,j+1} &= 1/6\Delta x \ . \end{aligned} \tag{1.11}$$

Then we can combine this time derivative with a flux as defined before. Terms $f_j/2 + f_{j+1}/2$ will contribute to the central differenced flux, while terms $T_{j+1/2}/2$ (defined after here) will appear only in dissipative terms and finally give the sixth-order dissipation:

$$\Phi(u_j,u_{j+1}) = \frac{u_j + u_{j+1}}{2} - \frac{\delta c}{2} T_{j+\frac{1}{2}} \tag{1.12}$$

According to the Pascal triangle, a fifth-order difference evaluated between j and $j+1$ can be written as follows ($C > 0$):

$$T_{j+1/2} = Cc(-u_{j-2} + 5u_{j-1} - 10u_j + 10u_{j+1} - 5u_{j+2} + u_{j+3}) \tag{1.13}$$

We choose the constant C as:

$$C = \frac{\delta}{60} \ .$$

in order to have the same level of dissipation as in the upwind case . Finally we get:

$$\begin{aligned} \Psi_j(U) \ = \ \frac{c}{2\Delta x}(& \quad C & & u_{j-3} \\ & + \quad (-6C) & & u_{j-2} \\ & + \quad (-1+15C) & & u_{j-1} \\ & + \quad (-20C) & & u_j \\ & + \quad (1+15)C & & u_{j+1} \\ & + \quad (-6C) & & u_{j+2} \\ & \quad C & & u_{j+3} \\ & & &) \end{aligned} \tag{1.14}$$

1.3 Time advancing stability

1.3.1 Explicit time stepping

Let us consider a time integration of the system $MU_t = AU$, with A the spatial approximation matrix and M the P1 finite element mass matrix. We can combine the above scheme with the standard six-stage Runge-Kutta scheme:

$$\begin{aligned} &U^{(0)} = U^n \\ &U^{(k)} = U^{(0)} + \tfrac{\Delta t}{N-k+1} M^{-1} \Psi \left(U^{(k-1)} \right), \quad k = 1 \dots N \\ &U^{n+1} = U^{(6)} \end{aligned} \tag{1.15}$$

The stability study of the scheme is made with the Fourier analysis. Let us include in equations (1.4) the Fourier mode: $\hat{u}_j^n = \overline{u}_k e^{ij\theta_k}$ where θ_k is the frequence parameter.
We obtain:

$$m_\theta \tfrac{d\hat{u}_j^n}{dt} = -(\hat{\Psi^\delta})_n^j$$

i.e

$$m_\theta \tfrac{d\hat{u}_j^n}{dt} = \lambda_\theta \hat{u}_j^n$$

with:

$$(\hat{\Psi^\delta})_n^j = \tfrac{c}{2\Delta x}(R_3 \cos(3\theta) + R_2 \cos(2\theta) + R_1 \cos(\theta) + R_0 + iI_1 \sin(\theta))\hat{u}_j^n$$

and

$$\begin{cases} R_3 = 2\delta C \\ R_2 = -12\delta C \\ R_1 = 30\delta C \\ R_0 = -20\delta C \\ I_1 = 2 \end{cases}$$

Because $\left(\hat{\Psi^\delta}\right)_n^j = -\lambda_\theta \hat{u}_j^n$, we have:

$$\lambda_\theta = -\frac{c}{2\Delta x}(R_3\cos(3\theta) + R_2\cos(2\theta) + R_1\cos(\theta) + R_0 + iI_1\sin(\theta))$$

We introduce the Courant number $\nu = \frac{c\Delta t}{\Delta x}$ and the amplification factor is $G_\theta = G_\theta(z_\theta^M)$ with $z_\theta^M = \frac{\lambda_\theta \Delta t}{m_\theta}$,where G_θ is the caracteristic polinomial of RK6, $G_\theta(z) = 1 + z + \frac{z^2}{2} + \frac{z^3}{6} + \frac{z^4}{24} + \frac{z^5}{120} + \frac{z^6}{720}$. We recall that the P1 finite element mass matrix M is a three-diagonal one, equal to M=Three-diag($\frac{1}{6}, \frac{2}{3}, \frac{1}{6}$) and we get:

$$m_\theta = \frac{1}{3}(2 + \cos(\theta))$$

Finaly, we have:

$$\begin{cases} z_\theta^M = -\frac{3\nu}{2(2+\cos(\theta))}(z_\theta^R + iz_\theta^I) \\ z_\theta^R = R_3\cos(3\theta) + R_2\cos(2\theta) + R_1\cos(\theta) + R_0 \\ z_\theta^I = I_1\sin(\theta) \end{cases}$$

The figure bellow illustrate the stability study for the explicit scheme RK6. We visualize the stability curve of the scheme for different values of the parameters.This stability curve is represented by the function:

$$g(\nu) = \max_{\theta\in[0,\pi]}(\|G_\theta\|) \tag{1.16}$$

As we can see on the figure, for RK6 our centred dissipated scheme is not stable.

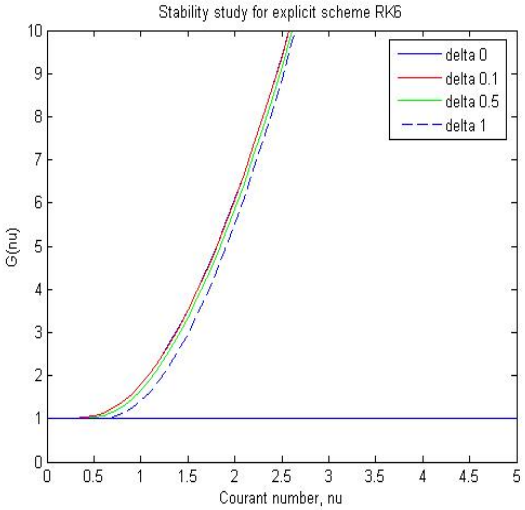

Figure 1.1. Stability study for different values of dissipation factor

1.3.2 Implicit time stepping

The purpose of this section is the convergence analysis of the implicite scheme. This can be also done with Fourier analysis. The computation is made on the same one-dimensional scalar conservation law. Let us use the implicite scheme like a δ-scheme:

$$T^n \delta U^{n+1} = \Delta t^n \Psi(U^n)$$

with $\delta U^{n+1} = U^{n+1} - U^n$ and T^n is the implicite matrix.
In case of a first order scheme, T^n represents the following three-diagonal matrix :

$$T^n = diag(-\nu, 1+\nu, 0)$$

With the Fourier analysis we obtain:

$$t_\theta = 1 + \nu(1 - \cos(\theta)) + i\nu \sin(\theta)$$

The amplification factor is then given by:

$$G(\Delta t) = \frac{t_\theta + z_\theta}{t_\theta}$$

We are must interested on behavior of the amplification factor when the time step Δt tends to $+\infty$ on the aim to know if the builds ones schemes are preconditionated at first ordre with satisfactory factors of convergence. Let us denote $\lim_{\Delta t \to \infty} G(\Delta t) = f_\theta(\delta)$. We are searching the Fourier's modes for different schemes witch maximises the functions $f_\theta(\delta) = 1 - \frac{1}{4(1-\cos(\theta))m_\theta}[(1-\cos(\theta))z_\theta^R + \sin(\theta)z_\theta^I] + i[\frac{\sin(\theta)z_\theta^R - (1-\cos(\theta))z_\theta^I}{4m_\theta(1-\cos(\theta))}]$. The results of stability are examined in the figures (1.2)(1.3)(1.4)(1.5)(1.6)(1.7)(1.8) bellow, where we can observe that our implicit scheme is inconditionally stable.Let us denote that the optimal value that minimise the gain function is for $\delta = 1$.

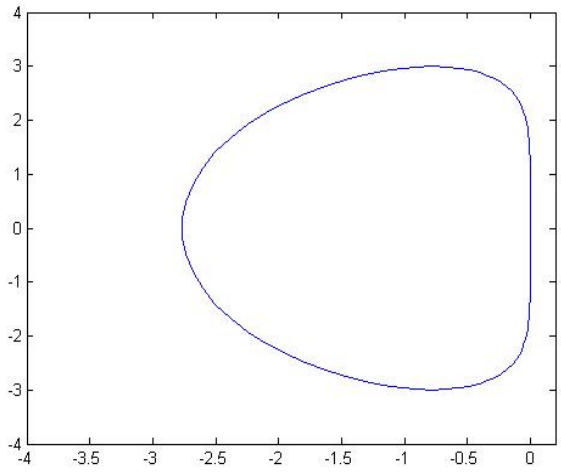

Figure 1.2. Stability domaine for $\nu = 1.73$ and $\delta = 1$

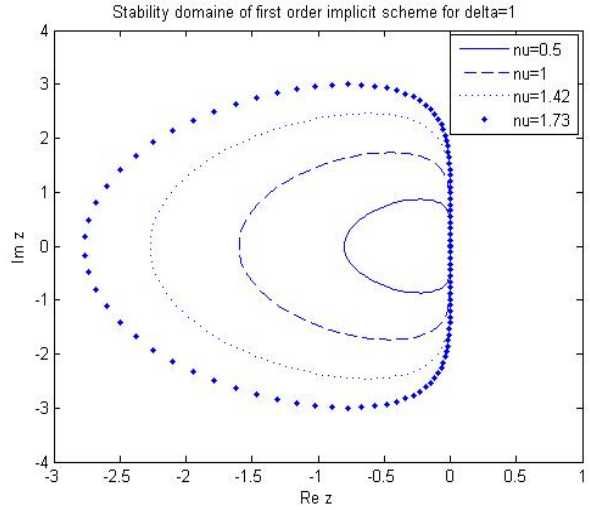

Figure 1.3. Stability domaine of first order implicit scheme for $\delta = 1$

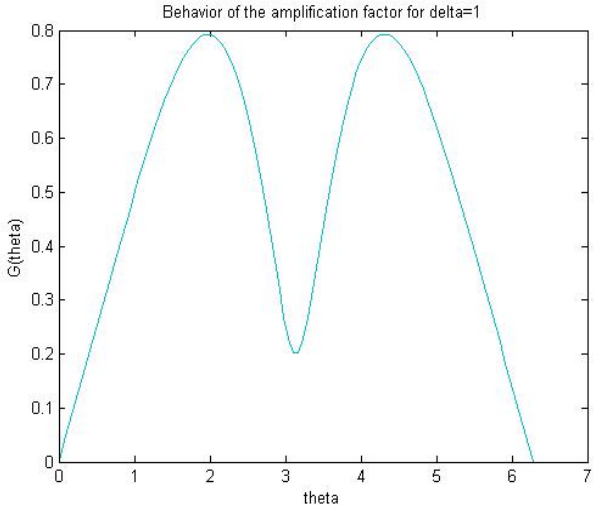

Figure 1.4. Gain function for $\delta = 1$

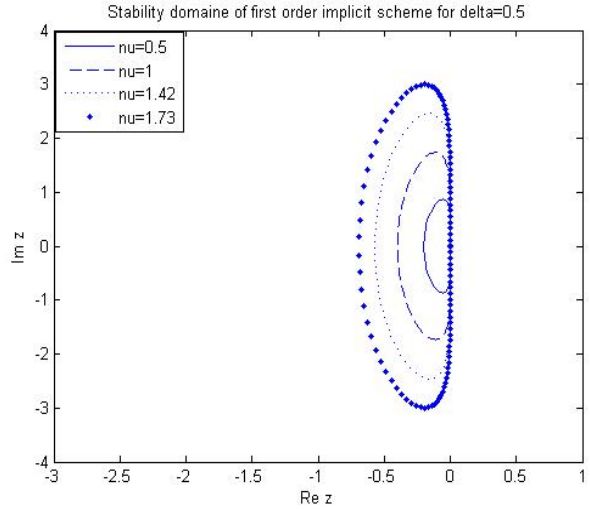

Figure 1.5. Stability domaine of first order implicit scheme for $\delta = 0.5$

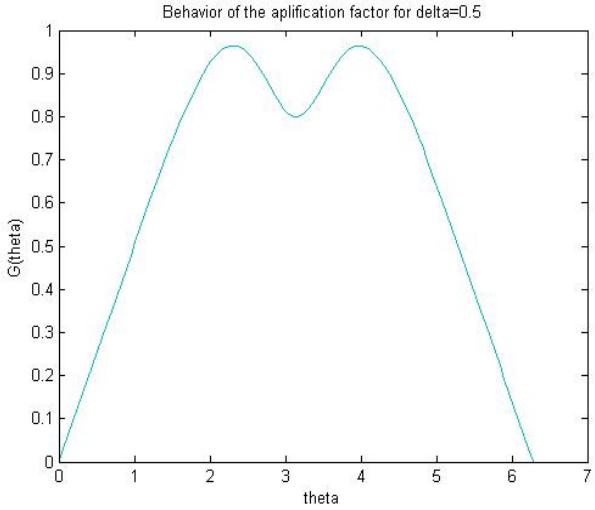

Figure 1.6. Gain function for $\delta = 0.5$

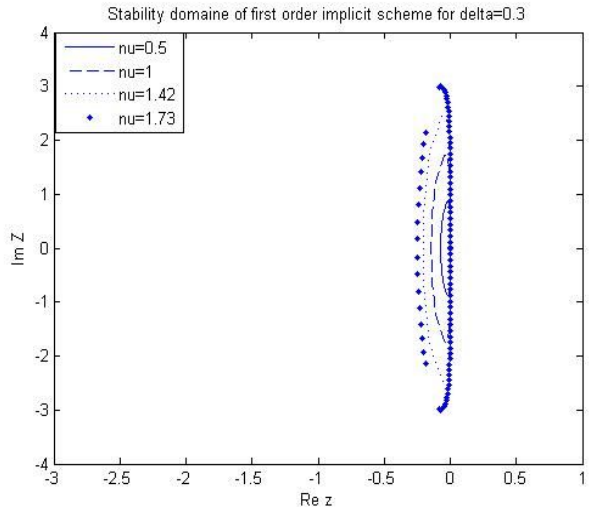

Figure 1.7. Stability domaine of first order implicit scheme for $\delta = 0.3$

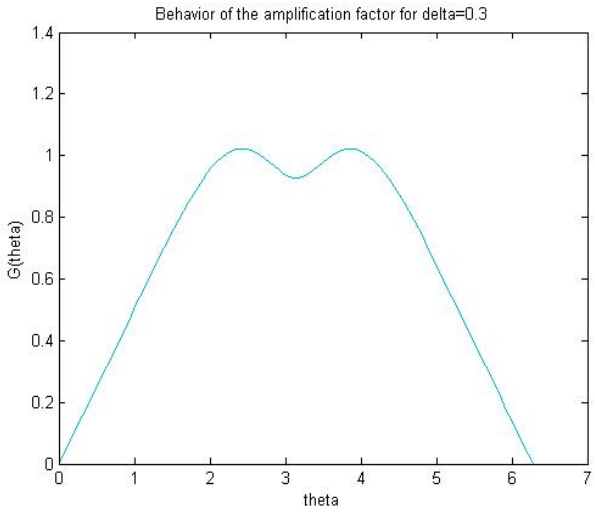

Figure 1.8. Gain function for $\delta = 0.3$

Chapter 2

Numerical Method

2.1 Introduction

In the present chapter the code AERO, used in the present study, is described. The code permits to solve the Euler equations, the Navier Stokes equations for laminar flows and to use different turbulence models for RANS, LES and hybrid RANS/LES approaches. The unknown quantities are the density, the components of the momentum and the total energy per unit volume. AERO employs a mixed finite-volume/finite-element formulation for the spatial discretization of the equations. Finite-volumes are used for the convective fluxes and finite-elements (P1) for the diffusive ones.

The resulting scheme is second order accurate in space. The equations can be advanced in time with explicit low-storage Runge-Kutta schemes. Also implicit time advancing is possible, based on a linearised method that is second order accurate in time.

2.2 Set of equations

In the AERO code the Navier Stokes equations are numerically normalised with the following reference quantities:

- $L_{ref} \Longrightarrow$ characteristic length of the flow
- $U_{ref} \Longrightarrow$ velocity of the free-stream flow
- $\rho_{ref} \Longrightarrow$ density of the free-stream flow
- $\mu_{ref} \Longrightarrow$ molecular viscosity of the free-stream flow

The flow variables can be normalised with the reference quantities as follows:

$$\rho^* = \frac{\rho}{\rho_{ref}} \qquad u_j^* = \frac{u_j}{U_{ref}} \qquad p^* = \frac{p}{p_{ref}}$$

$$E^* = \frac{E}{\rho_{ref} U_{ref}^2} \qquad \mu^* = \frac{\mu}{\mu_{ref}} \qquad t^* = t\,\frac{L_{ref}}{U_{ref}}\ . \tag{2.1}$$

The non-dimensional form of the Navier Stokes equations for the laminar case are reported in the following:

$$\begin{aligned}
\frac{\partial \rho^*}{\partial t^*} + \frac{\partial (\rho^* u_j^*)}{\partial x_j^*} &= 0 \\
\frac{\partial (\rho^* u_i^*)}{\partial t^*} + \frac{\partial \rho^* u_i^* u_j^*}{\partial x_j^*} &= -\frac{\partial p^*}{\partial x_i^*} + \frac{1}{Re}\frac{\partial \sigma_{ij}^*}{\partial x_j^*} \\
\frac{\partial (\rho^* E^*)}{\partial t^*} + \frac{\partial (\rho^* E^* u_j^*)}{\partial x_j^*} &= -\frac{\partial (p^* u_j^*)}{\partial x_j^*} + \frac{1}{Re}\frac{\partial (u_j^* \sigma_{ij}^*)}{\partial x_i^*} - \frac{\gamma}{RePr}\frac{\partial}{\partial x_j^*}\left[\mu^*\left(E^* - \frac{1}{2}u_j^* u_j^*\right)\right]
\end{aligned} \tag{2.2}$$

where the Reynolds number, $Re = U_{ref} L_{ref}/\nu$, is based on the references quantities, U_{ref} and L_{ref}, the Prandlt number, Pr, can be assumed constant for a gas and equal to:

$$Pr = \frac{C_p \mu}{k}$$

and $\gamma = C_p/C_v$ is the ratio between the specific heats at constant pressure and volume. Also the constitutive equations for the viscous stresses and the state equations may be written in non-dimensional form as follows:

$$\begin{aligned} \sigma_{ij}^* &= -\frac{2}{3}\mu^*\Big(\frac{\partial u_k^*}{\partial x_k^*}\delta_{ij}\Big) + \mu^*\Big(\frac{\partial u_i^*}{\partial x_j^*} + \frac{\partial u_j^*}{\partial x_i^*}\Big) \\ p^* &= (\gamma - 1)\rho^*\Big(E^* - \frac{1}{2}u_j^* u_j^*\Big) \ . \end{aligned} \tag{2.3}$$

In order to rewrite the governing equations in a compact form more suitable for the discrete formulation, the following unknown variables are grouped together in the $\boldsymbol{W}$ vector:
$\boldsymbol{W} = (\rho,\, \rho u,\, \rho v,\, \rho w,\, \rho E)^T$.
If two other vectors, $\boldsymbol{F}$ and $\boldsymbol{V}$ are defined as function of $\boldsymbol{W}$, as follows:

$$\boldsymbol{F} = \begin{pmatrix} \rho u & \rho v & \rho w \\ \rho u^2 + p & \rho uv & \rho uw \\ \rho uv & \rho v^2 + p & \rho vw \\ \rho uw & \rho vw & \rho w^2 + p \end{pmatrix}$$

and

$$\boldsymbol{V} = \begin{pmatrix} 0 & 0 & 0 \\ \sigma_{xx} & \sigma_{yx} & \sigma_{zx} \\ \sigma_{xy} & \sigma_{yy} & \sigma_{zy} \\ \sigma_{xz} & \sigma_{yz} & \sigma_{zz} \\ u\sigma_{xx} + v\sigma_{xy} + w\sigma_{xz} - q_x & u\sigma_{xy} + v\sigma_{yy} + w\sigma_{yz} - q_y & u\sigma_{xz} + v\sigma_{yz} + w\sigma_{zz} - q_z \end{pmatrix}$$

they may be substituted in (2.2), to get a different compact format of the governing equations which is the starting point for the derivation of the Galerkin formulation and of the discretization of the problem:

$$\frac{\partial \boldsymbol{W}}{\partial t} + \frac{\partial}{\partial x_j} F_j(\boldsymbol{W}) - \frac{1}{Re} \frac{\partial}{\partial x_j} V_j(\boldsymbol{W}, \nabla \boldsymbol{W}) = 0 \ . \tag{2.4}$$

It is important to stress that the vectors $\boldsymbol{F}$ and $\boldsymbol{V}$ are respectively the convective fluxes and the diffusive fluxes.

2.3 Spacial discretization

Spatial discretization is based on a mixed finite-volume/finite-element formulation. A finite volume upwind formulation is used for the treatment of the convective fluxes while a classical Galerkin finite-element centred approximation is employed for the diffusive terms .

The computational domain Ω is approximated by a polygonal domain Ω_h. This polygonal domain is then divided in N_t tetrahedrical elements T_i by a standard finite-element triangulation process:

$$\Omega_h = \bigcup_{i=1}^{N_t} T_i. \tag{2.5}$$

The set of elements T_i forms the grid used in the finite-element formulation. The dual finite-volume grid can be built starting from the triangulation following the medians method.

In the medians method a finite-volume cell is constructed around each node a_i of the triangulation, dividing in 4 sub-tetrahedra every tetrahedron having a_i as a vertex by means of the median planes. C_i is the union of the resulting sub-tetrahedra having a_i as a vertex and they have the following property:

$$\Omega_h = \bigcup_{i=1}^{N_c} C_i. \tag{2.6}$$

where N_c is the number of cells, which is equal to the number of the nodes of the triangulation.

Convective fluxes

Indicating the basis functions for the finite-volume formulation as follows:

$$\psi^{(i)}(P) = \begin{cases} 1 & \text{if } P \in C_i \\ 0 & \text{otherwise} \end{cases}$$

the Galerkin formulation for the convective fluxes is obtained by multiplying the convective terms of (2.4) by the basis function $\psi^{(i)}$, integrating on the domain Ω_h and using the divergence theorem. In this way the results are:

$$\iint_{\Omega_h} \Big(\frac{\partial F_j}{\partial x_j}\Big)\psi^{(i)}\,\mathrm{d}x\,\mathrm{d}y = \iint_{C_i} \frac{\partial F_j}{\partial x_j}\,\mathrm{d}\Omega = \int_{\partial C_i} F_j n_j\,\mathrm{d}\sigma$$

where $d\Omega$, $d\sigma$ and n_j are the elementary measure of the cell, of its boundary and the jth component of the normal external to the cell C_i respectively.
The total contribution to the convective fluxes is:

$$\sum_j \int_{\partial C_{ij}} \mathcal{F}(\boldsymbol{W},\vec{n})\,\mathrm{d}\sigma$$

where j are all the neighbouring nodes of i, $\mathcal{F}(\boldsymbol{W},\vec{n}) = F_j(\boldsymbol{W})n_j$, ∂C_{ij} is the boundary between cells C_i and C_j, and $\vec{n}$ is the outer normal to the cell C_i.

The basic component for the approximation of the convective fluxes is the Roe scheme, Ref. [13]:

$$\int_{\partial C_{ij}} \mathcal{F}(\boldsymbol{W},\vec{n})\,\mathrm{d}\sigma \simeq \Phi^R(W_i,W_j,\vec{\nu}_{ij})$$

where

$$\vec{\nu}_{ij} = \int_{\partial C_{ij}} \vec{n}\,\mathrm{d}\sigma$$

and W_k is the solution vector at the k-th node of the discretization.
The numerical fluxes, Φ^R, are evaluated as follows:

$$\Phi^R(W_i,W_j,\vec{\nu}_{ij}) = \underbrace{\frac{\mathcal{F}(W_i,\vec{\nu}_{ij}) + \mathcal{F}(W_j,\vec{\nu}_{ij})}{2}}_{centred} - \underbrace{\gamma_s \; d^R(W_i,W_j,\vec{\nu}_{ij})}_{upwinding}$$

where $\gamma_s \in [0,1]$ is a parameter which directly controls the upwinding of the scheme and

$$d^R(W_i,W_j,\vec{\nu}_{ij}) = \Big| \mathcal{R}(W_i,W_j,\vec{\nu}_{ij}) \Big| \frac{W_j - W_i}{2} \; . \tag{2.7}$$

$\mathcal{R}$ is the Roe matrix and is defined as:

$$\mathcal{R}(W_i,W_j,\vec{\nu}_{ij}) = \frac{\partial \mathcal{F}}{\partial \boldsymbol{W}}(\widehat{\boldsymbol{W}},\nu_{ij}) \tag{2.8}$$

where $\widehat{\boldsymbol{W}}$ is the Roe average between W_i and W_j.
The classical Roe scheme is obtained as a particular case by imposing $\gamma_s = 1$. The accuracy of this scheme is only $1st$ order. In order to increase the order of accuracy of the scheme the MUSCL (*Monotone Upwind Schemes for Conservation Laws*) reconstruction method, introduced by Van Leer, Ref. [16], is employed. This method expresses the Roe flux as a function of the extrapolated values of $\boldsymbol{W}$ at the interface between the two cells C_i and C_j, W_{ij} and W_{ji}:

$$\int_{\partial C_{ij}} \mathcal{F}(\boldsymbol{W},\vec{n}) \, \mathrm{d}\sigma \simeq \Phi^R(W_{ij},W_{ji},\vec{\nu}_{ij})$$

where W_{ij} and W_{ji} are defined as follows:

$$W_{ij} = W_i + \frac{1}{2}(\vec{\nabla}\boldsymbol{W})_{ij} \cdot \vec{ij} \; , \tag{2.9}$$

$$W_{ji} = W_j + \frac{1}{2}(\vec{\nabla}\boldsymbol{W})_{ji} \cdot \vec{ij} \; . \tag{2.10}$$

To estimate the gradients $(\vec{\nabla}\boldsymbol{W})_{ij} \cdot \vec{ij}$ and $(\vec{\nabla}\boldsymbol{W})_{ji} \cdot \vec{ij}$ the $V6$ scheme is used, Ref. [6]:

$$
\begin{aligned}
(\vec{\nabla}\boldsymbol{W})_{ij}\cdot\vec{ij} &= (1-\beta)(\vec{\nabla}\boldsymbol{W})^C_{ij}\cdot\vec{ij}) + \beta(\vec{\nabla}\boldsymbol{W})^U_{ij}\cdot\vec{ij}) + \\
&\quad \xi_c\left[(\vec{\nabla}\boldsymbol{W})^U_{ij}\cdot\vec{ij}) - 2(\vec{\nabla}\boldsymbol{W})^C_{ij}\cdot\vec{ij}) + (\vec{\nabla}\boldsymbol{W})^D_{ij}\cdot\vec{ij})\right] + \\
&\quad \xi_c\left[(\vec{\nabla}W)_M\cdot\vec{ij}) - 2(\vec{\nabla}W)_i\cdot\vec{ij}) + (\vec{\nabla}W)^D_j\cdot\vec{ij})\right] , \qquad (2.11)
\end{aligned}
$$

$$
\begin{aligned}
(\vec{\nabla}\boldsymbol{W})_{ji}\cdot\vec{ji} &= (1-\beta)(\vec{\nabla}\boldsymbol{W})^C_{ji}\cdot\vec{ij}) + \beta(\vec{\nabla}\boldsymbol{W})^U_{ji}\cdot\vec{ij}) + \\
&\quad \xi_c\left[(\vec{\nabla}\boldsymbol{W})^U_{ji}\cdot\vec{ij}) - 2(\vec{\nabla}\boldsymbol{W})^C_{ji}\cdot\vec{ij}) + (\vec{\nabla}\boldsymbol{W})^D_{ji}\cdot\vec{ij})\right] + \\
&\quad \xi_c\left[(\vec{\nabla}\boldsymbol{W})_{M'}\cdot\vec{ij}) - 2(\vec{\nabla}\boldsymbol{W})_i\cdot\vec{ij}) + (\vec{\nabla}\boldsymbol{W})^D_j\cdot\vec{ij})\right] , \qquad (2.12)
\end{aligned}
$$

where $(\vec{\nabla}\boldsymbol{W})_i$ and $(\vec{\nabla}\boldsymbol{W})_j$ are the nodal gradients at the nodes i and j respectively and are calculated as the average of the gradient on the tetrahedra $T \in C_i$, having the node i as a vertex. For example for $(\vec{\nabla}\boldsymbol{W})_i$ we can write:

$$
(\vec{\nabla}\boldsymbol{W})_i = \frac{1}{Vol(C_i)}\sum_{T\in C_i}\frac{Vol(T)}{3}\sum_{k\in T} W_k\vec{\nabla}\Phi^{(i,T)} \ . \qquad (2.13)
$$

where $\Phi^{(i,T)}$ is the P1 finite-element basis function defined before. $(\vec{\nabla}\boldsymbol{W})_M\cdot\vec{ij}$, for the 3D case, is the gradient at the point M in Fig. 2.1 and it is computed by interpolation of the nodal gradient values at the nodes contained in the face opposite to the upwind tetrahedron T_{ij}. $(\vec{\nabla}\boldsymbol{W})_{M'}\cdot\vec{ij}$ is the gradient at the point M' in Fig. 2.1 and it is evaluated in the same way as $(\vec{\nabla}\boldsymbol{W})_M\cdot\vec{ij}$. The coefficients β, ξ_c, ξ_d are parameters that control the combination of fully upwind and centred slopes. The V6 scheme is obtained by choosing them to have the best accuracy on cartesian meshes, Ref.[**?**]:

$$
\beta = 1/3, \qquad \xi_c - 1/30, \qquad \xi_d = -2/15 \ .
$$

An important variant of the above scheme involves a time derivative that is evaluated with the finite-element consistent mass matrix, expressed in terms of the usual P1 test functions as follows:

$$M_{ij} = \int \varphi_i \varphi_j d\nu$$

which carries an extra parameter ω equal to 1 when the matrix is from FEM, 0 when we keep the previous diagonal one:

$$M_{ij}^{\omega} = \omega \int \phi_i \phi_j \, dv + (1-\omega) M_i^{FVM} j$$
$$M_i^{FVM} j = Vol(C_i) \quad if \quad i = j, \;\; 0 \;\; else.$$

As in section 1.2 we can combine this time derivative with a flux and we get the mass matrix scheme :

$$\Phi(W_i, W_j, \vec{\nu_{ij}}) = \frac{\mathcal{F}(W_i, \vec{\nu_{ij}}) + \mathcal{F}(W_j, \vec{\nu_{ij}})}{2} - \frac{\delta_s}{2} \left| \mathcal{R}(W_i, W_j, \vec{\nu_{ij}}) \right| \Delta W_{ij} \qquad (2.14)$$

where:

$$\Delta W_{ij} = C(2(\vec{\nabla} W)_M . \vec{ij} - 5(\vec{\nabla} W)_{ij}^u . \vec{ij} + 6(\vec{\nabla} W)_{ij}^c . \vec{ij} - 5(\vec{\nabla} W)_{ij}^d . \vec{ij} + 2(\vec{\nabla} W)_{M'} . \vec{ij}) \; .$$

with $C = \frac{\delta}{60}$ following the study done for the 1D advection equation. A variant of this scheme is also investigated and consists in using a dissipation projected in $\vec{ij}$: $|\mathcal{R}(W_i, W_j, \vec{\nu_{ij}})|$ becomes $\left| \mathcal{R}(W_i, W_j, \tilde{\vec{\nu_{ij}}}) \right|$ in which $\tilde{\vec{\nu_{ij}}} = (\vec{\nu_{ij}} \frac{\vec{ij}}{\|\vec{ij}\|}) \frac{\vec{ij}}{\|\vec{ij}\|}$

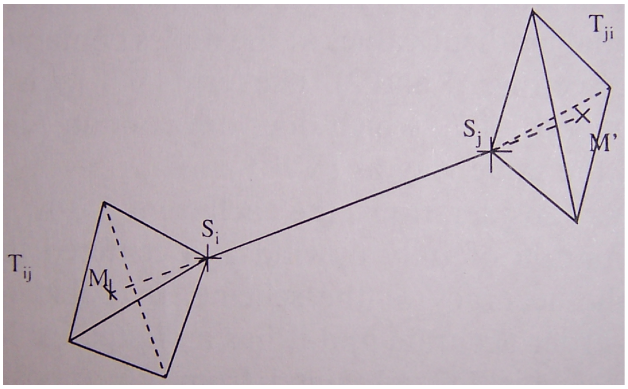

Figure 2.1. Sketch of points and elements involved in the computation of gradient

Diffusive fluxes

The P1 finite-element basis function, $\phi^{(i,T)}$, restricted to the tetrahedron T is assumed to be of unit value on the node i and to vanish linearly at the remaining vertexes of T. The Galerkin formulation for the diffusive terms is obtained by multiplying the diffusive terms by $\phi^{(i,T)}$ and integrating over the domain Ω_h:

$$\iint_{\Omega_h} \Big(\frac{\partial V_j}{\partial x_j}\Big)\phi^{(i,T)}\,\mathrm{d}\Omega = \iint_T \frac{\partial V_j}{\partial x_j}\phi^{(i,T)}\,\mathrm{d}\Omega\ .$$

Integrating by parts the right-hand side of Eq.(2.3) we obtain:

$$\iint_T \frac{\partial V_j}{\partial x_j}\phi^{(i,T)}\,\mathrm{d}\Omega = \iint_T \frac{\partial (V_j\phi^{(i,T)})}{\partial x_j}\,\mathrm{d}\Omega - \iint_T V_j\frac{\partial \phi^{(i,T)}}{\partial x_j}\,\mathrm{d}\Omega = \int_{\partial T} V_j\phi^{(i,T)}n_j\,\mathrm{d}\sigma - \iint_T V_j\frac{\partial \phi^{(i,T)}}{\partial x_j}\,\mathrm{d}\Omega\ . \tag{2.15}$$

In order to build the fluxes for the node i consistently with the finite-volume formulation, the contribution of all the elements having i as a vertex needs to be summed together as follows:

$$\sum_{T,i\,\in\,T}\Big(\int_{\partial T} V_j\phi^{(i,T)}n_j\,\mathrm{d}\sigma - \iint_T V_j\frac{\partial \phi^{(i,T)}}{\partial x_j}\,\mathrm{d}\Omega\Big) = -\sum_{T,i\,\in\,T}\iint_T V_j\frac{\partial \phi^{(i,T)}}{\partial x_j}\,\mathrm{d}\Omega + \int_{\Gamma_h=\partial\Omega_h}\phi^{(i,T)}V_jn_j\,\mathrm{d}\sigma\ . \tag{2.16}$$

In the P1 formulation for the finite-element method, the test functions, $\phi^{(i,T)}$, are linear functions on the element T and so their gradient is constant. Moreover, in the variational formulation the unknown variables contained in $\boldsymbol{W}$ are also approximated by their projection on the P1 basis function. For these reasons the integral can be evaluated directly.

2.4 Boundary conditions

Firstly, the real boundary Γ is approximated by a polygonal boundary Γ_h that can be split in two parts:

$$\Gamma_h = \Gamma_\infty + \Gamma_b \tag{2.17}$$

where the term Γ_∞ represents the far-fields boundary and Γ_b represents the body surface. The boundary conditions are set using the Steger-Warming formulation ([**?**]) on Γ_∞ and using slip or no-slip conditions on Γ_b.

2.5 Time advancing

Once the equations have been discretized in space, the unknown of the problem is the solution vector at each node of the discretization as a function of time, $\boldsymbol{W}_h(t)$. Consequently the spatial discretization leads to a set of ordinary differential equations in time:

$$\frac{d\boldsymbol{W}_h}{dt} + \Psi(\boldsymbol{W}_h) = 0 \tag{2.18}$$

where Ψ_i is the total flux, containing both convective and diffusive terms, of W_h through the i-th cell boundary divided by the volume of the cell.

Explicit time advancing

In the explicit case a N-step low-stockage Runge-Kutta algorithm is used for the discretization of Eq.(2.18):

$$\begin{cases} \boldsymbol{W}^{(0)} = \boldsymbol{W}^{(n)}, \\ \boldsymbol{W}^{(k)} = \boldsymbol{W}^{(0)} + \Delta t \ \alpha_k \ \Psi(\boldsymbol{W}^{(k-1)}), \ \ k = 1,\dots,N \\ \boldsymbol{W}^{(n+1)} = \boldsymbol{W}^{(N)}. \end{cases}$$

in which the suffix h has been omitted for sake of simplicity. Different schemes can be obtained varying the number of steps, N, and the coefficients α_k.

Implicit time advancing

For the implicit time advancing scheme in AERO the following second order accurate backward difference scheme is used:

$$\alpha_{n+1}\boldsymbol{W}^{(n+1)} + \alpha_n \boldsymbol{W}^{(n)} + \alpha_{(n-1)}\boldsymbol{W}^{(n-1)} + \Delta t^{(n)}\Psi(\boldsymbol{W}^{(n+1)}) = 0 \tag{2.19}$$

where the coefficients α_n can be expressed as follows:

$$\alpha_{n+1} = \frac{1+2\tau}{1+\tau}, \qquad \alpha_n = -1-\tau, \qquad \alpha_{n-1} = \frac{\tau^2}{1+\tau} \tag{2.20}$$

where $\Delta t^{(n)}$ is the time step used at the n-th time iteration and

$$\tau = \frac{\Delta t^{(n)}}{\Delta t^{(n-1)}}. \tag{2.21}$$

The nonlinear system obtained can be linearised as follows:

$$\begin{aligned}\alpha_{n+1}\boldsymbol{W}^{(n)} + \alpha_n \boldsymbol{W}^{(n)} + \alpha_{(n-1)}\boldsymbol{W}^{(n-1)} + \Delta t^{(n)}\Psi(\boldsymbol{W}^{(n)}) = \\ - \left[\alpha_{n+1} + \delta t^{(n)}\frac{\partial \Psi}{\partial \boldsymbol{W}}(\boldsymbol{W}^{(n)})\right](\boldsymbol{W}^{(n+1)} - \boldsymbol{W}^{(n)}).\end{aligned} \tag{2.22}$$

Following the defect-correction approach, the jacobians are evaluated using the 1st order flux scheme (for the convective part), while the explicit fluxes are composed with 2nd order accuracy. The resulting linear system is solved by a Schwarz method.

Chapter 3

Turbulence Models

3.1 Direct Numerical Simulation

Turbulent flows are always characterized by an unsteady and three-dimensional behaviour and can be described by the Navier-Stokes equations.

For a compressible flow, if a thermally and calorically perfect gas is considered and if the body forces are absent or negligible, the governing equations may be written as (Einstein notation used):

$$\begin{aligned}
\frac{\partial \rho}{\partial t} + \frac{\partial (\rho u_j)}{\partial x_j} &= 0, \\
\frac{\partial (\rho u_i)}{\partial t} + \frac{\partial (\rho u_i u_j)}{\partial x_j} &= -\frac{\partial p}{\partial x_i} + \frac{\partial \sigma_{ij}}{\partial x_j}, \\
\frac{\partial (\rho E)}{\partial t} + \frac{\partial (\rho E u_j)}{\partial x_j} &= -\frac{\partial (p u_j)}{\partial x_j} + \frac{\partial (u_j \sigma_{ij})}{\partial x_i} - \frac{\partial q_j}{\partial x_j}, \\
p &= \rho R T, \\
E &= C_v T + \frac{1}{2} u_i u_i.
\end{aligned} \tag{3.1}$$

In the above equations density, temperature, pressure, total energy for unit mass and specific heat at constant volume are represented respectively by ρ, T,p, E and C_v. In the last equation R is equal to $\Re/m$ where $\Re$ is the universal constant of

perfect gas and m is the moles mass. By assuming the flow to be Newtonian and under the Stokes hypothesis, the viscous stress tensor results:

$$\sigma_{ij} = -\frac{2}{3}\mu\frac{\partial u_k}{\partial x_k}\delta_{ij} + \mu\Big(\frac{\partial u_i}{\partial x_j} + \frac{\partial u_j}{\partial x_i}\Big) \tag{3.2}$$

where δ_{ij} is the kronecker delta and the viscosity coefficient μ is, generally, a function of the temperature. Moreover, the Fourier law is adopted to model the heat flux:

$$q_i = -K\frac{\partial T}{\partial x_i} \tag{3.3}$$

where K is the conduction coefficient for the gas and is generally a function of the temperature. The system of equations quoted above can be numerically integrated for every turbulent flow provinding a sufficiently fine spatial and temporal resolution. Because of the non-linearities of the equation system, the problem is characterized by a large range of spatial and temporal turbulent scales which are function of Reynolds number. The kinetic turbulent energy is extracted by the greater scales of turbulence and then it is transferred to smaller and smaller scales where is dissipated, as predicted by the *Energy Cascade* concept. A typical distribution of energy in a turbulent flow as function of the wave-number, n, which is inversely proportional to the spatial scale, is represented in Fig. 3.1.

Fig. 3.1 gives information about the mean-energy of the turbulent structures which have the same dimensions. These structures can be splitted in the following ranges:

- *energy-containing range*, which contains the largest vortical turbulent structures
- *inertial range* or *subrange*, which contains vortexes of intermediate dimensions
- *dissipation range*, which contains the smallest structures.

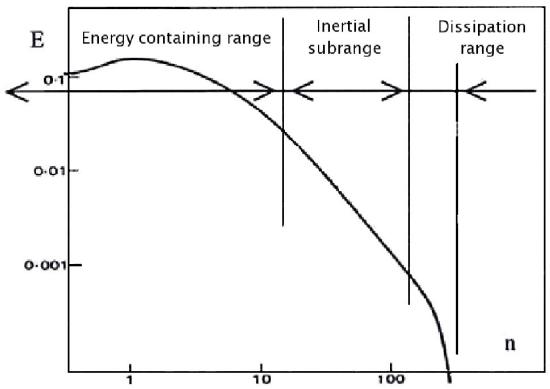

Figure 3.1. Typical energy spectrum of a turbulent boundary layer

To estimate the characteristic time and the spatial dimensions of turbulence, the results of the *Universal Equilibrium Theory* of Kolmogorov can be used. For homogeneous and isotropic turbulence, the spatial orders of magnitude of the largest scales, L, and of the smallest scale in the flow, l_k, are related as follows:

$$\frac{L}{l_k} = Re^{3/4} \tag{3.4}$$

where $Re = \frac{UL}{\nu}$ is the Reynolds number of the flow, based on L and on a integral velocity, which can be assumed similar to the velocity of the largest scales. The previous relation clearly show that the separation between large and small scales increases with the Reynolds number. The largest scales of turbulence carry most of the turbulence kinetic energy so they are responsible of the turbulent transport. The smallest scales are responsible of most of the dissipation of kinetic energy, so even if their contribution to the kinetic energy is negligible in comparison with the largest scales they must be considered to obtain accurate results. To this purpose, the single computational cell must have the dimensions of the smallest turbulent scales and the computational domain must be enough large to contain the largest flow structures. Thus, the number of nodes in the whole domain (N) increases with the Reynolds number as follows:

$$N = Re^{9/4} \ . \tag{3.5}$$

As the Reynolds number increases, strong limitations for numerical simulation occur due to the time resolution requirements. The governing equations, indeed, must be advanced for a global time interval, ΔT_c, of the order of the largest temporal scales, T_c, and the temporal step must be small enough to capture the smallest temporal scales, of the order of t_k. The ratio between the largest and the smallest temporal scales necessary to simulate the flux is clearly Re dependent:

$$\frac{T_c}{t_k} = Re^{1/2} \tag{3.6}$$

Thus, if the global time step is constant, the number of temporal steps needed to cover all the range ΔT_c quickly increases, as the Reynolds number is increased.
The huge computational resources needed to directly simulate turbulent flows at high Reynolds numbers ($Re > 10^4$) are not affordable at present. For this reason, the direct numerical simulation (DNS) is only used for low Reynolds number flows in simple geometries. On the other hand the information which can be obtained in DNS, is much larger than the one required in industrial or engineering problems. Thus, other simplified models have been developed in order to obtain the required information at a significantly reduced computational cost. Reynolds Averaged Navier-Stokes (RANS), Large Eddy Simulation (LES), Detached Eddy Simulation (DES) and Limited Numerical Scales (LNS) are examples of these models.
It is important to stress, however, that DNS permits to obtain a large amount of information on turbulence, which is useful to devise and validate turbulent models for the closure of RANS and LES. Thus, DNS plays an important role for the industrial numerical simulation, although indirect.

3.2 Reynolds-Averaged Navier-Stokes equations

The Navier-Stokes equations for compressible flows of (calorically and thermally) perfect Newtonian gases are considered here, written in a conservative form (see Eqs. 3.1). The RANS equations are derived by first decomposing the variables (f) in a statistic or time-averaged part ($\overline{f}$) and a fluctuating one (f'); this decomposition, called the Reynolds decomposition, is then introduced in the Navier-Stokes equations which are successively averaged. Since compressible flows are considered a density-weighted average (Favre average, $\widetilde{f}$) is introduced to suppress correlations of the form $\overline{\rho' f'}$:

$$\widetilde{f} = \frac{\overline{\rho f}}{\overline{\rho}} \quad . \tag{3.7}$$

The averaged flow variables are the unknowns of the RANS problem. However, the RANS equations also contain second-order moments of the flow fluctuations. As well known, these terms must be expressed as a function of the averaged flow variables in order to close the problem. In the present work, the RANS part is closed using the classical $k-\varepsilon$ model and the *Low-Reynolds* $k-\varepsilon$ model discussed in the following. The final form of the RANS equations for compressible flows, with the assumption of an eddy-viscosity model and ignoring some terms write as follows:

$$\begin{aligned}
&\frac{\partial \overline{\rho}}{\partial t} + \left(\overline{\rho}\widetilde{u}_i\right)_{,i} = 0 \quad , \\
&\left(\overline{\rho}\widetilde{u}_i\right)_{,t} + \left(\rho\widetilde{u}_i\widetilde{u}_j\right)_{,j} = -\frac{\partial \overline{p}}{\partial x_i} + \left((\mu+\mu_t)\widetilde{P_{ij}}\right)_{,j} \quad , \\
&\left(\overline{E}\right)_{,t} + \left[\widetilde{u}_j\left(\overline{E}+\overline{p}\right)\right]_{,j} = \left[\widetilde{u}_i\widetilde{\sigma}_{ij}\right]_{,j} + \left[\widetilde{u}_i R_{ij}\right]_{,j} + \left[\frac{\mu_t}{\sigma_k}\frac{\partial k}{\partial x_j}\right]_{,j} + \\
&\qquad\qquad \left[C_p\left(\frac{\mu}{Pr} + \frac{\mu_t}{Pr_t}\right)\frac{\partial \widetilde{T}}{\partial x_j}\right]_{,j} = 0 \quad ,
\end{aligned} \tag{3.8}$$

where $\widetilde{\sigma}_{ij}$ is the averaged viscous-stress tensor, $\overline{E}$ the averaged total energy per unit volume (turbulence included), μ the molecular viscosity of the gas, C_p the specific heat at constant pressure, p the thermodynamic pressure, T the gas temperature, Pr_t the turbulent Prandtl number ($Pr_t = 0.9$ in the present work) and μ_t is the RANS viscosity which depends on the type of closure used (see Sec.3.2.1 or Sec. 3.2.2). Finally, the constitutive equation for P_{ij} and the averaged state equations of the gas write as follows:

$$P_{ij} = \frac{\partial u_i}{\partial x_j} + \frac{\partial u_j}{\partial x_i} - \frac{2}{3}\frac{\partial u_k}{\partial k}\delta_{ij} \tag{3.9}$$

$$\overline{p} = \overline{\rho} R \widetilde{T} \quad , \tag{3.10}$$

$$\widetilde{e} = C_v \widetilde{T} \quad , \tag{3.11}$$

where R is the gas constant and C_v its specific heat at constant volume.

3.2.1 Standard $k - \varepsilon$ model

The $k - \varepsilon$ model is an eddy-viscosity 2 equation model in which the turbulent eddy-viscosity μ_t is defined as a function of the turbulent kinetic energy k and the turbulent dissipation rate of energy ε as follows:

$$\mu_\mathrm{t} = C_\mu \rho \frac{k^2}{\varepsilon} \quad , \tag{3.12}$$

where C_μ is a constant equal to 0.09. The Reynolds stress tensor is the main unclosed term of the RANS equations, and is modeled according to the Boussinesq assumption:

$$R_{ij} = -\overline{\rho}\widetilde{u_i'u_j'} \simeq \mu_\mathrm{t} \underbrace{\left[\frac{\partial \widetilde{u}_i}{\partial x_j} + \frac{\partial \widetilde{u}_j}{\partial x_i} - \frac{2}{3}\frac{\partial \widetilde{u}_k}{\partial k}\delta_{ij}\right]}_{\widetilde{P}_{ij}} - \frac{2}{3}\overline{\rho} k \delta_{ij} \quad , \tag{3.13}$$

δ_{ij} being the Kronecker symbol.

The spatial distribution of k and ϵ is estimated by solving the following transport equations:

$$\frac{\partial \overline{\rho} k}{\partial t} + \left(\overline{\rho}\widetilde{u}_j k\right)_{,j} = \left[\left(\mu + \frac{\mu_\mathrm{t}}{\sigma_k}\right)\frac{\partial k}{\partial x_j}\right]_{,j} + R_{ij}\frac{\partial \widetilde{u}_i}{\partial x_j} - \overline{\rho}\varepsilon \quad , \tag{3.14}$$

$$\frac{\partial \overline{\rho} \varepsilon}{\partial t} + \left(\overline{\rho}\varepsilon\widetilde{u}_j\right)_{,j} = \left[\left(\mu + \frac{\mu_\mathrm{t}}{\sigma_\epsilon}\right)\frac{\partial \varepsilon}{\partial x_j}\right]_{,j} + C_{\epsilon 1}\left(\frac{\varepsilon}{k}\right)R_{ij}\frac{\partial \widetilde{u}_i}{\partial x_j} - C_{\epsilon 2}\overline{\rho}\frac{\varepsilon^2}{k} \quad . \tag{3.15}$$

where $C_{\epsilon 1}$, $C_{\epsilon 2}$, σ_k and σ_ϵ are the model parameters and usually are set as follow:

$$C_{\epsilon 1} = 1.44 \qquad C_{\epsilon 2} = 1.92 \qquad \sigma_k = 1.0 \qquad \sigma_\epsilon = 1.3$$

3.2.2 Low Reynolds $k - \varepsilon$ model

The Low Reynolds $k - \varepsilon$ model used here is that proposed by Goldberg (Ref. [**?**]). The Reynolds stress tensor has the same form of that used in the standard $k - \varepsilon$ model (Eq.3.13) but here the turbulent eddy-viscosity μ_t is defined as follows:

$$\mu_t = C_\mu f_\mu \rho \frac{k^2}{\epsilon} \tag{3.16}$$

Here $C_\mu = 0.09$ as in the standard $k-\varepsilon$ model and f_μ is a damping function chosen as follows:

$$f_\mu = \frac{1 - e^{-A_\mu R_t}}{1 - e^{-R_t^{1/2}}} max(1,\psi^{-1}) \tag{3.17}$$

where $\psi = R_t^{1/2}/C_\tau$, $R_t = k^2/(\nu\varepsilon)$ is the turbulence Reynolds number ($\nu = \mu/\rho$) and $A_\mu = 0.01$; k and ε are determinated by the following transport equations:

$$\frac{\partial \overline{\rho} k}{\partial t} + (\overline{\rho}\widetilde{u}_j k)_{,j} = \left[\left(\mu + \frac{\mu_t}{\sigma_k}\right)\frac{\partial k}{\partial x_j}\right]_{,j} + R_{ij}\frac{\partial \widetilde{u}_i}{\partial x_j} - \overline{\rho}\varepsilon \quad , \tag{3.18}$$

$$\frac{\partial \overline{\rho} \varepsilon}{\partial t} + (\overline{\rho}\varepsilon\widetilde{u}_j)_{,j} = \left[\left(\mu + \frac{\mu_t}{\sigma_\epsilon}\right)\frac{\partial \varepsilon}{\partial x_j}\right]_{,j} + \left(C_{\epsilon 1} R_{ij}\frac{\partial \widetilde{u}_i}{\partial x_j} - C_{\epsilon 2}\overline{\rho}\varepsilon + E\right) T_\tau^{-1} \quad . \tag{3.19}$$

Where T_τ is the realisable time scale and is expressed as follows:

$$T_\tau = \frac{k}{\epsilon} max(1,\psi^{-1}) \tag{3.20}$$

this time scale is k/ε at large R_t (hence large ψ) but becomes the Kolmogorov scale, $C_\tau(\nu/\varepsilon)^{1/2}$, for $R_t << 1$. The value of C_τ is assumed to be 1.41, $C_{\epsilon 1} = 1.42$, $C_{\epsilon 2} = 1.83$, . The extra source term E in the ε equation is designed such that its near-wall limit cancels the corresponding non-zero destruction term and is computed as follows:

$$E = \rho A_E V (\varepsilon T_\tau)^{0.5} \xi \tag{3.21}$$

where $A_E = 0.3$, $V = max(\sqrt{k}, (\nu\varepsilon)^{0.25})$ and $\xi = max(\frac{\partial k}{\partial x_i}\frac{\partial \tau}{\partial x_i}, 0)$, with $\tau = k/\varepsilon$.

3.3 Large Eddy Simulation

The large-eddy simulation approach (LES) is intermediate between DNS, where all fluctuations are resolved, and the statistical simulations based on RANS, where only the mean flow is resolved. In LES the severe Reynolds number restrictions of DNS are bypassed by directly simulating the large scales (GS) only and supplying the effect of the missing small scales (SGS) by a so-called sub-grid model. This is obtained by filtering the Navier-Stokes equations in space, in order to eliminate the flow fluctuations smaller then the filter size. In this way, the new unknowns of the problem become the filtered flow variables. Like for RANS, due to the non-linearity of the original problem, the new equations contain additional unknown terms, the so-called sub-grid scale (SGS) terms, representing the effect of the eliminated small scales on the filtered equations. In order to close the problem, these terms must be modelled. However, due to the fact that the small unresolved scales are often simpler in nature than the inhomogeneous large motions and do not significantly depend on the large scale motion, rather simple closure models may work well for many applications. Another advantage of this method is the possibility of directly simulating the largest scales, which are usually more interesting from the engineering point of view. Computationally, LES clearly is less demanding than DNS, but in general much more expensive than RANS. The reason is that, independently of the problem to be solved, LES always requires fully three-dimensional and unstationary calculations even for flows which are two-dimensional in the mean. Moreover LES, like DNS, needs to be carried out for long periods of time to obtain stable and significant statistics. For these reasons, LES should provide better results for the analysis of complex three-dimensional and time-dependent problems for which the RANS approach frequently fails, in particular when large flow separation is present.
The utilisation of LES for engineering problems is still not very extensive, but in the last years the interest in this method has largely increased.

3.3.1 SGS modeling

The energy-containing large scales structures (GS) mainly contribute for the turbulent transport while the dissipative small scale motions (SGS) carry most of the vorticity and act as a sink of turbulent kinetic energy. For high Reynolds numbers the dissipative part of the spectrum becomes clearly separated from the low wave-number range, in a way shown by Eq. (3.4). Some of the significant differences between GS and SGS scales are summarised in Tab. 3.1, Ref. [12].

To illustrate the role of SGS models, it is useful to consider possible consequences

GS turbulence	**SGS turbulence**
Produced by mean flow	Produced by larger eddies
Depends on boundaries	Universal
Ordered	Chaotic
Requires deterministic description	Can be modelled statistically
Inhomogeneous	Homogeneous
Anisotropic	Isotropic
Long-lived	Short-lived
Diffusive	Dissipative
Difficult to model	Easier to model

Table 3.1. Qualitative differences between GS turbulence and SGS turbulence

if turbulent simulation are performed with insufficient resolution. In this case the viscous dissipation in the flow cannot properly be accounted for. This will typically result in an accumulation of energy at the high wave-number end of the spectrum which reflect a distorted equilibrium state between production and dissipation of turbulent kinetic energy. For sufficiently high Reynolds numbers (or sufficiently coarse grids) the discrete representation of the flow even becomes essentially inviscid and the non-linear transfer of energy can lead to an unbounded growth of turbulence intensities and eventually to numerical instability of the computation.

3.3.2 Filtered equations of the motion

In LES any dependent variable of the flow, f, is split into a GS part, $\overline{f}$, and a SGS part, f':

$$f = \overline{f} + f' \tag{3.22}$$

Generally, the GS component, $\overline{f}$, represents that part of the turbulent fluctuation which remains after some smoothing which has been applied to the flow field. As done in Sec.3.2 it is convenient to define a density weighted filter since it allows to partially recover the formal structure of the equations of the incompressible problem. This filter is defined as in Eq. (3.7)

Applying the filtering operation to the Navier-Stokes equations, Eq. (3.1), yields the equations of motion of the GS flow field. Like in RANS the filtering of the non linearities is of particular interest since it gives rise to additional unknowns terms. For LES of compressible flows, the filtered form of the equations of motion for a thermally and calorically perfect gas is the following:

$$\begin{aligned}
\frac{\partial \overline{\rho}}{\partial t} + \frac{\partial (\overline{\rho}\tilde{u}_j)}{\partial x_j} &= 0 \\
\frac{\partial (\overline{\rho}\tilde{u}_i)}{\partial t} + \frac{\partial (\overline{\rho}\tilde{u}_i\tilde{u}_j)}{\partial x_j} &= -\frac{\partial \overline{p}}{\partial x_i} + \frac{\partial (\mu \tilde{P}_{ij})}{\partial x_j} - \frac{\partial M_{ij}^{(1)}}{\partial x_j} + \frac{\partial M_{ij}^{(2)}}{\partial x_j} \\
\frac{\partial (\overline{\rho}\tilde{E})}{\partial t} + \frac{\partial [(\overline{\rho}\tilde{E} + \overline{p})\tilde{u}_j}{\partial x_j} &= \frac{\partial (\tilde{u}_j \tilde{\sigma}_{ij})}{\partial x_i} - \frac{\partial \tilde{q}_j}{\partial x_j} + \frac{\partial}{\partial x_j}\Big(Q_j^{(1)} + Q_j^{(2)} + Q_j^{(3)}\Big).
\end{aligned} \tag{3.23}$$

In the momentum equation the sub-grid terms are represented by the terms $M_{ij}^{(i)}$ which can be defined as follows:

$$M_{ij}^{(1)} = \overline{\rho u_i u_j} - \overline{\rho}\tilde{u}_i\tilde{u}_j \tag{3.24}$$

$$M_{ij}^{(2)} = \overline{\mu P_{ij}} - \mu \tilde{P}_i j \tag{3.25}$$

where P_{ij} is defined in Eq.3.9. $M_{ij}^{(1)}$ takes into account the momentum transport of the sub-grid scales and $M_{ij}^{(2)}$ represents the transport of viscosity due to the sub-grid scales fluctuations.

In the energy equation the sub-grid term are represented by the terms $Q_j^{(i)}$ which can be defined as follows:

$$Q_j^{(1)} = \left[\tilde{u}_i\left(\overline{\rho}\tilde{E} + \overline{p}\right) - \overline{u_i(\rho E + p)}\right] \tag{3.26}$$

$$Q_j^{(2)} = \overline{\left(\mu P_{ij} u_j\right)} - \left(\mu \tilde{P}_{ij}\tilde{u}_j\right) \tag{3.27}$$

$$Q_j^{(3)} = \overline{K\frac{\partial T}{\partial x_j}} - K\frac{\partial \tilde{T}}{\partial x_j} \tag{3.28}$$

$Q_j^{(1)}$ represents three distinct physical effects:

- the transport of energy E due to small scales fluctuations;
- the change of the internal energy due to the sub-grid scale compressibility $\left(p\frac{\partial u_j}{\partial x_j}\right)$;
- the dissipation of energy due to sub-grid-scale motions in the pressure field $\left(u_j\frac{\partial p}{\partial x_j}\right)$;

$Q_j^{(2)}$ takes in account the dissipative effect due to the sub-grid scale transport of viscosity; $Q_j^{(3)}$ takes in account the heat transfer caused by the motion of the neglected sub-grid scales.

3.3.3 Subgrid Scale model

Smagorinsky's model

The Smagorinsky model is an example of closure models (ref.[15]). We assume that low compressibility effects are present in the SGS fluctuations and that heat transfer and temperature gradients are moderate. The retained SGS term in the momentum equation is thus the classical SGS stress tensor:

$$M_{ij} = \rho\overline{u_i u_j} - \bar{\rho}\tilde{u}_i\tilde{u}_j \tag{3.29}$$

where the over-line denotes the grid filter and the tilde the density-weighted Favre filter (Eq.3.7). The isotropic part of M_{ij} can be neglected under the assumption of low compressibility effect in the SGS fluctuations. The deviatoric part, T_{ij}, may be expressed by an eddy viscosity term, in accordance with the Smagorinsky model extended to compressible flow:

$$T_{ij} = -2\mu_s\Big(\tilde{S}_{ij} - \frac{1}{3}\tilde{S}_{kk}\Big), \tag{3.30}$$

$$\mu_s = \bar{\rho}C_s\Delta^2|\tilde{S}|. \tag{3.31}$$

where $S_{ij} = \frac{1}{2}\Big(\frac{\partial u_i}{\partial x_j} + \frac{\partial u_j}{\partial x_i}\Big)$ is the resolved strain rate tensor, μ_s is the SGS viscosity, Δ is the filter width, C_s is a constant which must be assigned a priori and $|\tilde{S}| = \sqrt{\tilde{S}_{ij}\tilde{S}_{ij}}$. The width of the filter is defined for every grid elements, l, as follows:

$$\Delta^{(l)} = Vol_j^{1/3} \tag{3.32}$$

where Vol_j is the volume of the $j-th$ grid element.
In the energy equation the effect of the SGS fluctuations has been modified by the introduction of a constant SGS Prandtl number to be assigned a priori:

$$Pr_{sgs} = C_p\frac{\mu_s}{K_{sgs}} \tag{3.33}$$

where K_{sgs} is the SGS conductivity coefficient and it takes into account the diffusion of total energy caused by the SGS fluctuation. In the filtered energy equation, the term K_{sgs} is added to the molecular conductivity coefficient.
Experiments pointed out that a C_s constant valor brings a lot of problems, like a wrong asintotic behaviour in the near wall region (τ_{ij} different from zero) and the impossibility of turbulent energy passage from little to large scales, cause the first

ones bring only and effect of energy dissipation. This problem has been partially solved with the introduction of a dynamic version of Smagorinsky model, in which C_s is locally obtained using the smallest scales computed. This is due to a particular algebraic identity and the use of a test filter coarser than the one used to filter Navier Stokes equations (Germano et al., 1991). This approach solves most of the problems resulting with a static eddy viscosity model closure, although numerical instability may appear due to high fluctuations of the C_s coefficient that may bring to a local negative viscosity. Composite eddy viscosity - scale similarity closure models (Zang et al.,1993) keep the good results of the classical dynamic eddy viscosity models drastically reducing instability problems. A limit for LES is due to the assumption frequently made in SGS modeling that the cut-off of the filter is in the inertial range and this, for high Reynolds flows, implies huge computational costs.

Another way to solve the behaviour problem in the near wall region is to use different expression of the SGS viscosity. The Vreman's and WALE model are such exemple of subgrid-scale closure.

Vreman's model

The Vreman's model [**?**] is designed with first-order derivatives and so is not more complicated than the Smagorinsky's model. This model is designed to give a zero eddy viscosity when zero theoretical value is expected and to adapt to the local level of turbulent activity, while it does not need more than the local filter width and the first-order derivatives of the velocity field.

The eddy viscosity μ_v of the Vreman's model is defined by:

$$\mu_v = c(\frac{B_\beta}{\alpha_{ij}\alpha_{ij}})^{\frac{1}{2}} \tag{3.34}$$

with

$$\alpha_{ij} = \partial\tilde{u_j}/\partial x_i$$

$$\beta_{ij} = \Delta^2\alpha_{mi}\alpha_{mj}$$

$$B_\beta = \beta_{11}\beta_{22} - \beta_{12}^2 + \beta_{11}\beta_{33} - \beta_{13}^2 + \beta_{22}\beta_{33} - \beta_{23}^2$$

The constant $c \approx 2.5C_s^2$ where C_s denotes the Smagorinsky constant.

The Vreman's SGS model has been validated first on a transitional and turbulent mixing layer at high Reynolds number and then on a turbulent channel fow at $Re_\tau = 360$. An appropriate transitional and near-wall flow behaviour was found with this model which, moreover seems to be robust in high Reynolds number simulations.
It has been also shown more accurate than the Smagorinsky's model in homogeneous turbulence.

WALE model

The Wall-Adapting Local Eddy -Viscosity (WALE) SGS model proposed by Nicoud and Ducros [**?**] is based on the square of the velocity gradient tensor. Improvements compared to the classical Smagorinsky's model are firstly the property to give a zero value of the eddy-viscosity near a wall without using a dynamic procedure, then to produce zero eddy-viscosity in case of a pure shear and finally the property to detect all the turbulence structures relevant for the kinetic energy dissipation.

The eddy-viscosity term μ_w of the model is defined by:

$$\mu_w = C_w \Delta^2 \frac{(\overline{S_{ij}}^d \overline{S_{ij}}^d)^{\frac{3}{2}}}{(S_{ij}S_{ij})^{\frac{5}{2}} + (\overline{S_{ij}}^d \overline{S_{ij}}^d)^{\frac{5}{4}}} \tag{3.35}$$

with

$$\overline{S_{ij}}^d = \frac{1}{2}(\overline{g_{ij}}^2 + \overline{g_{ji}}^2) - \frac{1}{3}\delta_{ij}\overline{g_{kk}}^2$$

is the symmetric part of the tensor $\overline{g_{ij}}^2 = \overline{g_{ik}g_{kj}}$, where $\overline{g_{ij}} = \partial\tilde{u}_i/\partial x_j$
and in which the constant C_w is set to 0.1.

The performance of the WALE model has been in particular illustrated for a freely decaying isotropic turbulence and for a turbulent pipe flow using a hybrid mesh [**?**].

3.4 Variational Multiscale approach for Large Eddy Simulation

A new approach to LES based on a variational multiscale(VMS)framework was recently introduced in Hughes et al. The VMS-LES differs fundamentally from the traditional LES in a number of ways. In this new approach, one does not filter the Navier-Stokes equations but uses instead a variational projection. This is an important difference because as performed in the traditional LES, filtering works as well with periodic boundary conditions but raises mathematical issues in wall-bounded flows. The variational projection avoids this issues. Furthermore, the VMS-LES method separates the scales a priori-that is, before the simulation is started. And most importantly, it models the effect of the unresolved-scales only in the equations representing the smallest resolved-scales, and not in the equations for the large scales. Consequently, in the VMS-LES, energy is extracted from the fine resolved-scales by a traditional model such as Smagorinsky eddy viscosity model, but no energy is directly extracted from the large structures in te flow. For this reason, one can reasonably hope to obtain a better behavior near walls, and less dissipation in the presence of large coherent structures.

A less fundamental, yet noteworthy, difference between the VMS-LES and traditional LES methods is that the VMS-LES approach leads to governing equations that are written in terms of the original (or undecomposed) flow variables and the modeled effect of the unresolved-scales on the smallest resolved one, whereas the classical LES formulation leads to governing equations that are written in terms of the filtered flow variables and modeled subgrid-scales. Hence, in the traditional LES formulation, one first filters the Navier-Stokes equations, then decomposes the flow variables into their filtered and fluctuating parts in the subgrid-tensor, then faces the issues of modeling the subgrid-scales. In the VMS-LES approach, one does not have to decompose into space-averaged and fluctuating parts each occurence in the Navier-Stokes equations of each flow variable because the final

equations are expected to be expressed in terms of the importance as it can be exploited to bypass the modeling of some fluctuating quantities, as will be illustrated here for compressible turbulent flows.

The initial developement of the VMS-LES method focused on incompressible turbulent flows, regular grids, and spectral discretisations where the separaton a priori of the scales is simple to achieve. For finite element approximations, a hierarchical basis approach and an alternative method based on cell agglomeration were recently proposed for separating a priori the coarse- and fine-scales. In most cases, the VMS-LES method was applied mainly to homogeneous isotropic incompressible turbulence, and recently to incompressible turbulent channel flows, fo witch it demonstrated an improvement over the traditional LES method.

In this Variational Multiscale approach for Large Eddy Simulation (VMS-LES) approach the flow variables are decomposed as follows:

$$w_i = \underbrace{\overline{w}_i}_{LRS} + \underbrace{w'_i}_{SRS} + {w_i}^{SGS} \tag{3.36}$$

where $\overline{w}_i$ are the large resolved scales (LRS), w'_i are the small resolved scales (SRS) and ${w_i}^{SGS}$ are the unresolved scales. This decomposition is obtained by variational projection in the LRS and SRS spaces respectively. In the present study, we follow the VMS approach proposed in Ref.[5] for the simulation of compressible turbulent flows through a finite volume/finite element discretization on unstructured tetrahedral grids. If ψ_l are the N finite-volume basis functions and ϕ_l the N finite-element basis fonctions associated to the used grid,in order to obtain the VMS flow decomposition in Eq. (3.36), the finite dimensional spaces $\mathcal{V}_{FV}$ and $\mathcal{V}_{FE}$, respectively spanned by ψ_l and ϕ_l, can be in turn decomposed as follows [5]:

$$\mathcal{V}_{FV} = \overline{\mathcal{V}}_{FV} \bigoplus \mathcal{V}'_{FV} \; ; \quad \mathcal{V}_{FE} = \overline{\mathcal{V}}_{FE} \bigoplus \mathcal{V}'_{FE} \tag{3.37}$$

in which $\bigoplus$ denotes the direct sum and $\overline{\mathcal{V}}_{FV}$ and $\mathcal{V}'_{FV}$ are the finite volume spaces

associated to the largest and smallest resolved scales, spanned by the basis functions $\overline{\psi_l}$ and ψ'_l; $\overline{\mathcal{V}}_{FE}$ and $\mathcal{V}'_{FE}$ are the finite element analogous. In Ref.[5] a projector operator P in the LRS space is defined by spatial average on macro cells in the following way:

$$\overline{\boldsymbol{W}} = P(\boldsymbol{W}) = \sum_k \underbrace{\left(\frac{Vol(C_k)}{\sum_{j \epsilon I_k} Vol(C_j)} \sum_{j \epsilon I_k} \psi_j \right)}_{\overline{\psi}_k} \boldsymbol{W}_k \tag{3.38}$$

for the convective terms, discretized by finite volumes, and:

$$\overline{\boldsymbol{W}} = P(\boldsymbol{W}) = \sum_k \underbrace{\left(\frac{Vol(C_k)}{\sum_{j \epsilon I_k} Vol(C_j)} \sum_{j \epsilon I_k} \phi_j \right)}_{\overline{\phi}_k} \boldsymbol{W}_k \tag{3.39}$$

for the diffusive terms, discretized by finite elements. In both Eqs. (3.38) and (3.39), $I_k = \{j / C_j \in C_{m(k)}\}$, $C_{m(k)}$ being the macro-cell containing the cell C_k. The macro-cells are obtained by a process known as agglomeration [8]. The basis functions for the SRS space are clearly obtained as follows: $\psi'_l = \psi_l - \overline{\psi}_l$ and $\phi'_l = \phi_l - \overline{\phi}_l$.

A key feature of the VMS-les approach is that the modeled influence of the unresolved scales on large resolved ones is set to zero, and so the SGS model is added only to the smallest resolved scales (which models the dissipative effect of the unresolved scales on small resolved ones). This leads to the following equations after semi-discretizations [5].

$$
\begin{aligned}
\int_{C_i} \frac{\partial \rho}{\partial t} \mathrm{d}\Omega + \int_{\partial C_i} \rho \vec{V}.\vec{n} \mathrm{d}\Gamma &= 0 \\
\int_{C_i} \frac{\partial \rho \vec{V}}{\partial t} \mathrm{d}\Omega + \int_{\partial C_i} \rho \vec{V} \otimes \vec{V} \vec{n} \mathrm{d}\Gamma + \int_{\partial C_i} p \vec{n} \mathrm{d}\Gamma & \\
+ \frac{1}{Re} \int_{\Omega} \sigma \nabla \Phi_i \mathrm{d}\Omega + \frac{1}{Re} \int_{\Omega} \tau^{'} \nabla \Phi_i^{'} \mathrm{d}\Omega &= 0 \\
\int_{C_i} \frac{\partial E}{\partial t} \mathrm{d}\Omega + \int_{\partial C_i} (E+p) \vec{V}.\vec{n} \mathrm{d}\Gamma + \int_{\Omega} \sigma \vec{V}.\nabla \Phi_i \mathrm{d}\Omega & \\
+ \frac{\gamma}{RePr} \int_{\Omega} \nabla e.\nabla \Phi_i \mathrm{d}\Omega + \frac{\gamma}{RePr_t} \int_{\Omega} \mu_t^{'} \nabla e^{'}.\nabla \Phi_i^{'} \mathrm{d}\Omega &= 0
\end{aligned}
\tag{3.40}
$$

where e denotes the internal energy ($E = e + \frac{1}{2}\vec{V}^2$) and $\tau^{'}$ is the small resolved scales SGS stress giben by:

$$\tau^{'} = \mu^{'} + (2S_{ij}^{'} - \frac{2}{3} S_{kk}^{'} \delta_{ij})$$

with $S_{ij}^{'} = \frac{1}{2}(\frac{\partial u_i^{'}}{\partial x_j} + \frac{\partial u_j^{'}}{\partial x_i})$ and $\mu_t^{'}$, the small resolved scales eddy viscosity (which depends pn the chosen SGS model).

One can notice that the laminar Navier-Stokes equations are recovered by substituting $\tau^{'} = 0$ and $\mu_t^{'} = 0$ in Eq. (3.40) above an that the SGS model is recovered by substituting $\tau^{'} = \tau$, $\mu_t^{'} = \mu_t$, $e^{'} = e$ and $\Phi_i^{'} = \Phi_i$ in the equations, where τ and μ_t denote the usual SGS stress tensor and SGS eddy viscosity, respectively.

More details about this VMS-LES methodology can be found in Ref. [5] and [2].

Chapter 4

Applications

4.1 Gaussian translation

In mathematics, a gaussian function (named after Carl Friedrich Gauss) is a function of the form:

$$f(x) = a \exp^{\frac{-(x-b)^2}{2c^2}}$$

for some real constants a, b and $c > 0$. The graph of a gaussian is a characteristic symmetric " bell shape curve " that quickly falls towards plus/minus infinity.
For our study we consider the gaussian function :

$$\rho(x,y,z,0) = 1 + \exp^{-150(x+0,3)}$$

We're interested on the behavior of the gaussian while we'll translate it using the following schemes: Mass Matrix Central Differencing Non Projected and Projected scheme, Masse Lumping V6 scheme. If the scheme is very dissipative then the gaussian will be dissipated too and the same thing for the dispersion.
The code AERO is used for the computation of the gaussian translation for regular mesh and irregular (strong variations of the local mesh size) one too.

In the regular case, we can observe in the figures 4.1 and 4.2 witch represents the gaussian translation for Mass Matrix Central Diff scheme and Mass Lumping V6 scheme that the translation is well predicted.In the irregular case, for Mass Matrix Central Diff schemes (see figures 4.3,4.5)the gaussian is well translated, but for Mass Lumping V6 scheme (see figure 4.4)we have some perturbations.

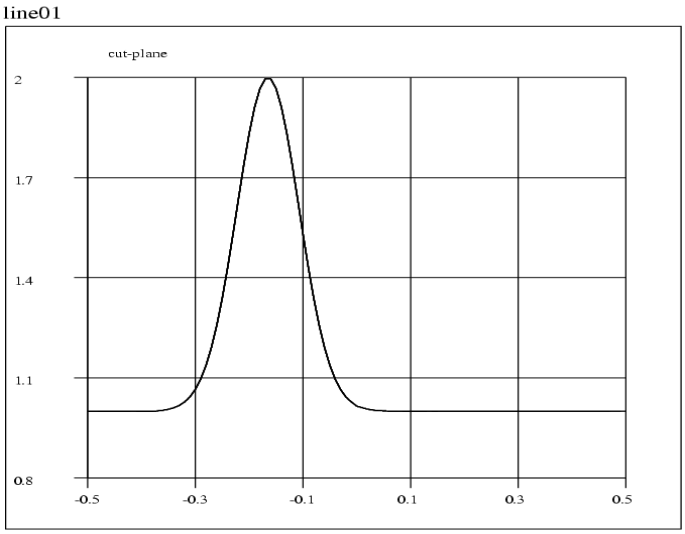

Figure 4.1. Gaussian translation for Mass Matrix Central Diff Projected scheme on regular mesh

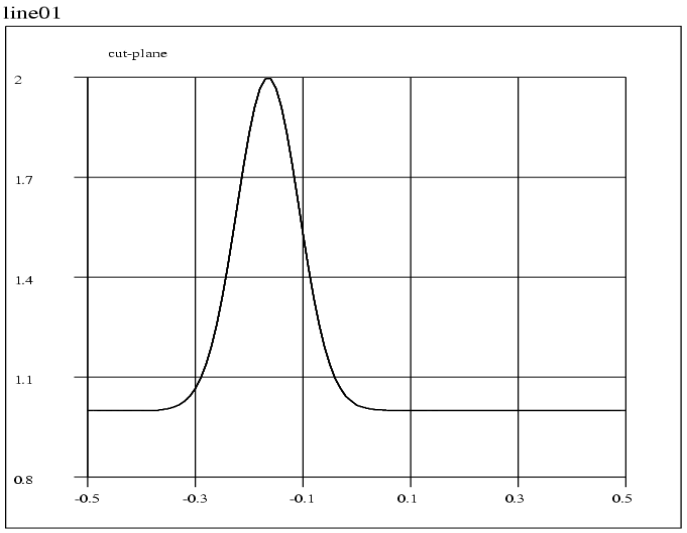

Figure 4.2. Gaussien translation for Mass Lumping V6 sheme on regular mesh

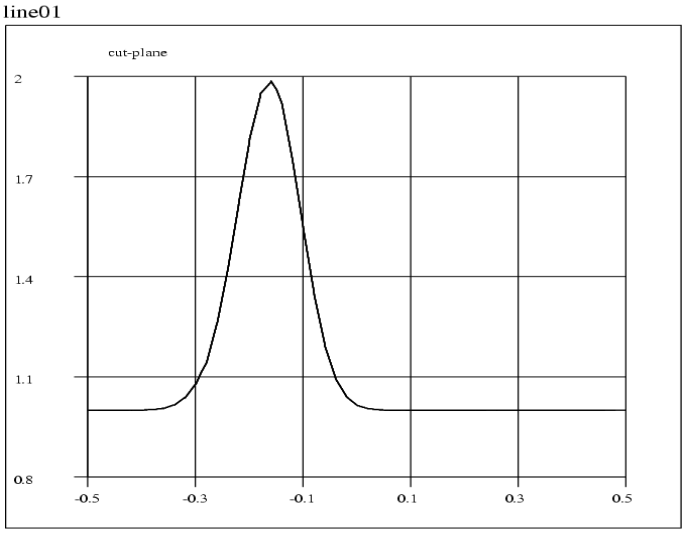

Figure 4.3. Gaussian translation for Mass Matrix Central Diff Projected scheme on irregular mesh

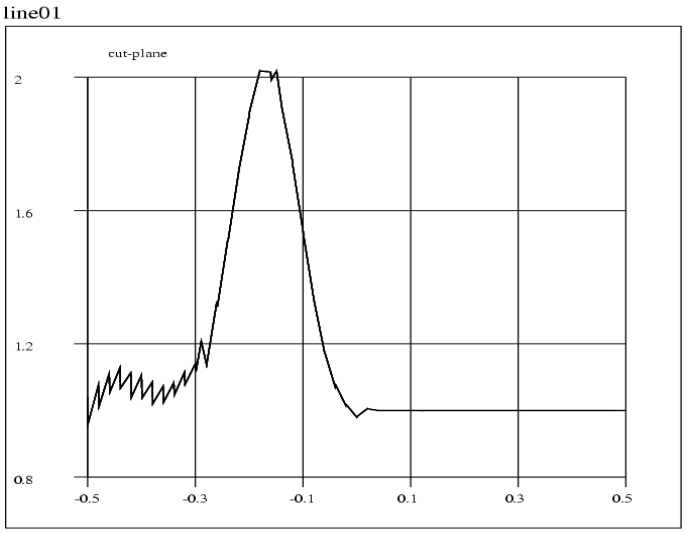

Figure 4.4. Gaussian translation for Mass Lumping V6 sheme on irregular mesh

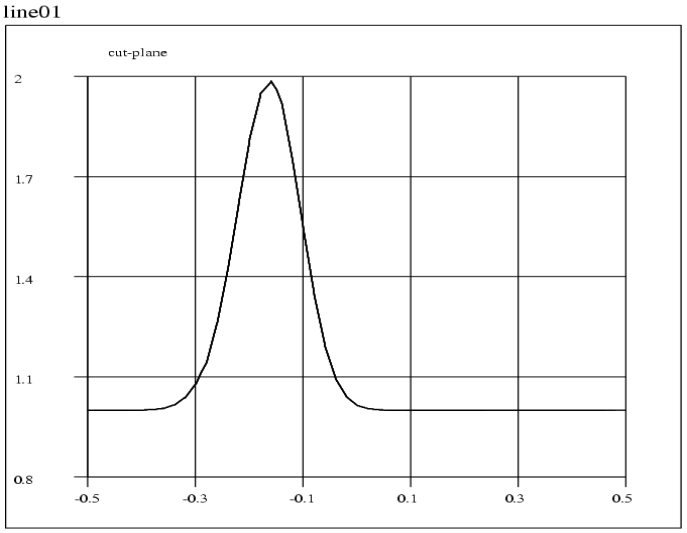

Figure 4.5. Gaussian translation for Mass Matrix Central Diff NonProjected scheme on irregular mesh

4.2 Flow around a circular cylinder at $Re_D = 3900$

VMS-LES is performed to simulate the flow past a circular cylinder at Mach number $M_\infty = 0.1$ and at a subcritical Reynolds number Re_D of 3900 ($\mathrm{Re}_D = \frac{u_\infty D}{\nu}$) based on cylinder diameter D and free-steam velocity u_∞. The computational domain as shown in Figure 4.6 is $-10 \leq x/D \leq 25$, $-20 \leq y/D \leq 20$ and $-\pi/2 \leq z/D \leq \pi/2$ where x, y and z denote the streamwise, transverse and spanwise direction respectively. The characteristics of the domain are the following:

$$L_i/D = 10, \quad L_0/D = 25, \quad H_y/D = 20 \quad \text{and} \quad H_z/D = \pi$$

The cylinder of unit diameter is centered on (x,y) = (0,0).

The flow domain is discretized by an unstructured tetrahedral grid which consists of approximatively 2.9×10^5 nodes. The averaged distance of the nearest point to the cylinder boundary is $0.017D$ which corresponds to $y^+ \approx 3.31$.

For the purpose of these simulations, the Steger-Warming conditions are imposed at the inflow and outflow as well as on the upper and lower surface ($y = \pm H_y$). In the spanwise direction periodic boundary conditions is applied. On the cylinder surface no-slip boundary conditions are set.

To investigate the influence of different schemas on the VMS-LES approach with a SGS Wale model, different simulations are carried out.The preconditioning used for this simulations is the Roe-Turkel solver. The schemes presented in this section are used with a numerical viscosity parameter γ set to 0.3 and to 1.

Simulation	Turbulence model	Numerical scheme	γ	CFL
Simu1	**VMS-LES wale**	**MassMatrix V6**	**1**	**20**
Simu2	**VMS-LES wale**	**MassMatrix Central Diff NonProjected**	**1**	**20**
Simu3	**VMS-LES wale**	**MassLump Central Diff NonProjected**	**1**	**20**
Simu3	**VMS-LES wale**	**MassLump Central Diff NonProjected**	**0.3**	**20**
Simu3	**VMS-LES wale**	**MassLump Central Diff Projected**	**0.3**	**20**
Simu3	**VMS-LES wale**	**MassLump V6**	**0.3**	**20**

Table 4.1. Simulations

The CFL number has been chose so that a vortex shedding cycle is sampled in

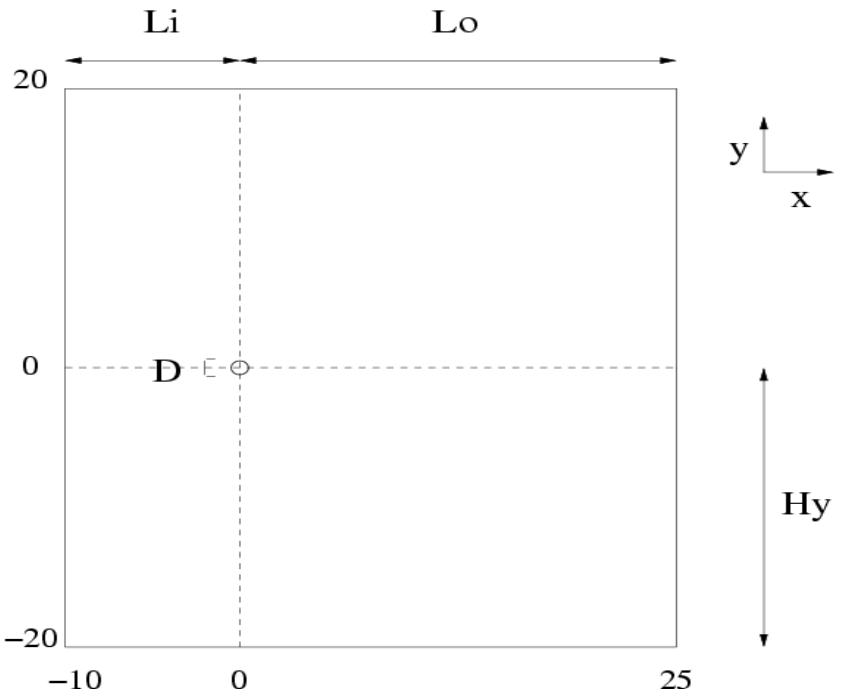

Figure 4.6. Computational domain

a little less than 1000 time steps.The drag and lift history of the simulations are shown in Figure 4.23,4.24,4.26and Figure 4.25 respectively. Time-averaged values and turbulence parameters are summarized in Table 4.2 and compared to data from experiments of Son and Hanratty , Norberg , Cardell and Williamson . $\overline{C_d}$ denotes the mean drag coefficient, $C_d^{'}$ and $C_l^{'}$ respectively the root mean square values of the drag and lift, St the Strouhal number.

As shown in the table bellow, for the Mass Matrix V6 ($\gamma = 1$)and Mass Lumping V6 ($gamma = 0.3$) schemes the Strouhal number is in good agreement with the experimental values, and we notice that for the Mass Matrix Central Differencing Non Projected and Projeted schemes the parameters are less well predicted.We also observe that the mean drag coefficient is smaller that the experimental data for

Simulation	*gamma*	*St*	$\overline{C_d}$	C'_d	C'_l	
Mass Lump Central Diff NonProjeted	**1**	**0.2372**	**0.7868**	**0.0156**	**0.0488**	
Mass Matrix Central Diff NonProjeted	**1**	**0.0113**	**0.7635**	**0.0167**	**0.0433**	
Mass Matrix V6	**1**	**0.2171**	**1.0892**	**0.0421**	**0.4663**	
Mass Matrix Central Diff Non Projeted	**0.3**	**0.0063**	**0.0004**	**0.0000**	**0.0001**	
Mass Matrix Central Diff Projeted	**0.3**	**0.0064**	**0.0004**	**0.0000**	**0.0002**	
Mass Lump V6	**0.3**	**0.2151**	**1.2307**	**0.0639**	**0.592**	
Exp. [10]		0.215±0.05	0.99±0.05			

Table 4.2. Flow parameters for $\gamma = 1$ or $\gamma = 0.3$ and CFL=20

Mass Lumping Central Diff Non Projected scheme and Mass Matrix Central Differencing Non Projected and Projected (for $\gamma = 1$ and $\gamma = 0.3$)scheme and larger than the experiment data for Mass Matrix V6 and Mass Lumping V6 scheme. The results show that the Masse Matrix V6 scheme improves the quality of the simulation, since all parameters are almost well predicted.
Figures (4.7),(4.8),(4.9),(4.10) show the time-averaged streamwise velocity on the centerline direction of the simulations from table 4.2.

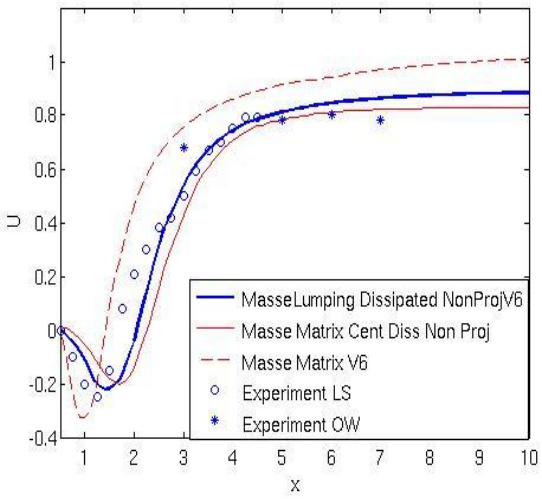

Figure 4.7. Time-averaged streamwise velocity on the centerline direction,experiments:Lourenco ans Shih(LS) and Ong and Wallace (OW)

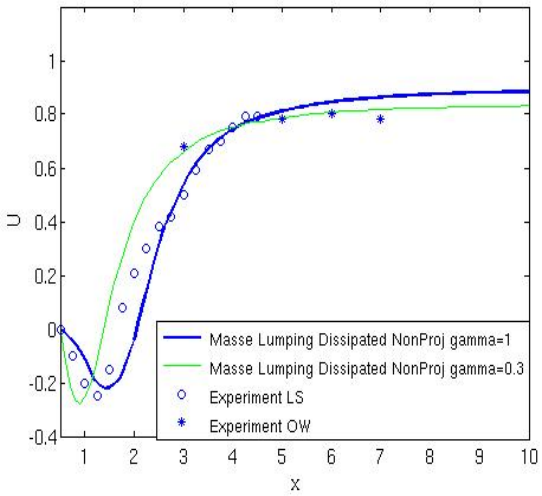

Figure 4.8. Time-averaged streamwise velocity on the centerline direction,experiments:Lourenco ans Shih(LS) and Ong and Wallace (OW)

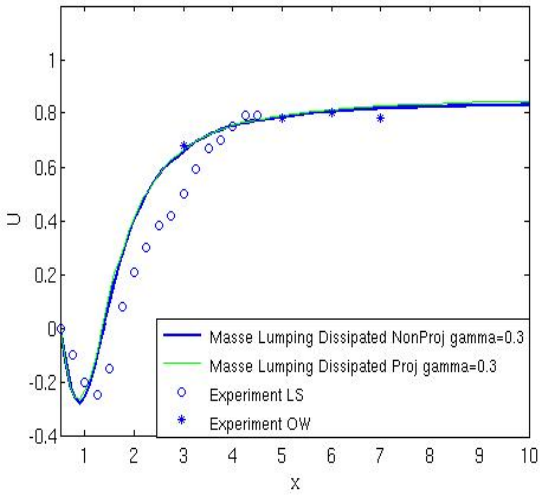

Figure 4.9. Time-averaged streamwise velocity on the centerline direction,experiments:Lourenco ans Shih(LS) and Ong and Wallace (OW)

We can observe here that the Masse Lumping Central Diff NonProj scheme for $\gamma = 1$ is the best scheme that follows the experimental results.

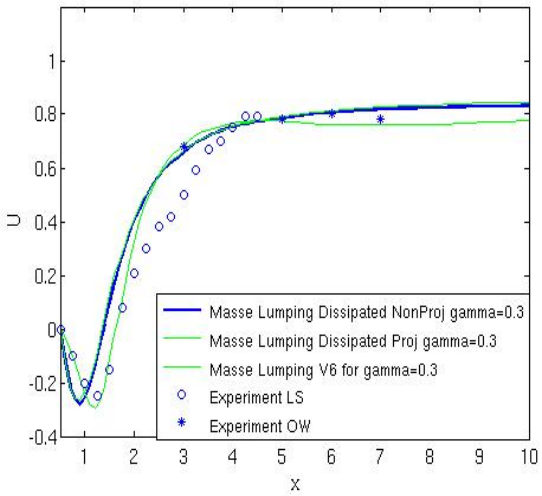

Figure 4.10. Time-averaged streamwise velocity on the centerline direction,experiments:Lourenco ans Shih(LS) and Ong and Wallace (OW)

Figures (4.11),(4.12),(4.13),(4.14)shows the pressure distribution on the cylinder surface averaged in time on homogeneous z direction.

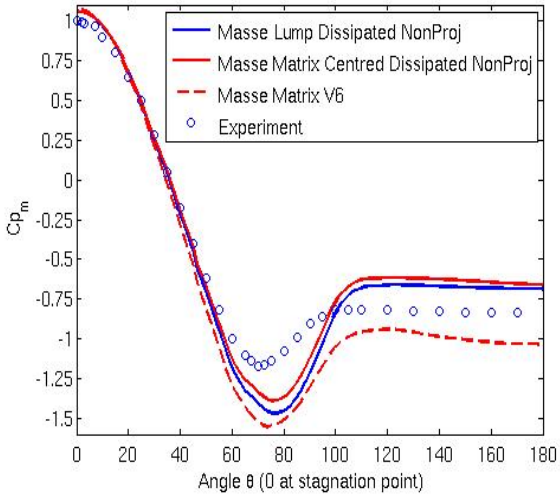

Figure 4.11. Time-averaged and z-averaged pressure distribution on the surface of the cylinder, experiment: Norberg

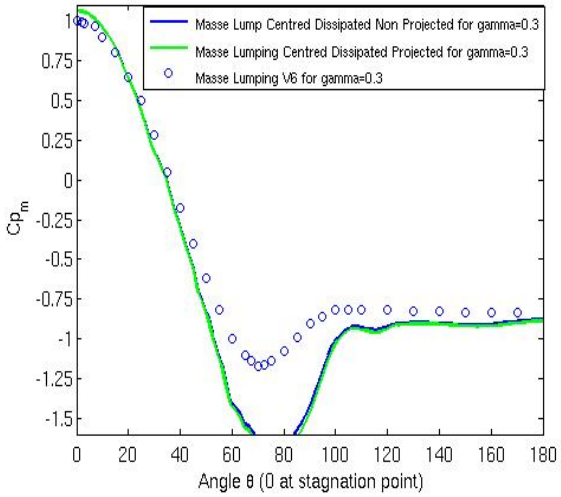

Figure 4.12. Time-averaged and z-averaged pressure distribution on the surface of the cylinder, experiment: Norberg

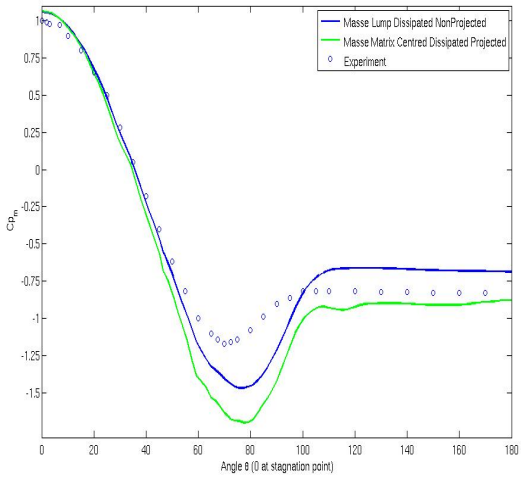

Figure 4.13. Time-averaged and z-averaged pressure distribution on the surface of the cylinder, experiment: Norberg

For Mass Matrix Central Diff Non Projected scheme and Mass Lumping Central Diff Non Projected scheme for $\gamma = 1$ the results are very close to each other on the whole cylinder but they don't match with the experimental data. Watching

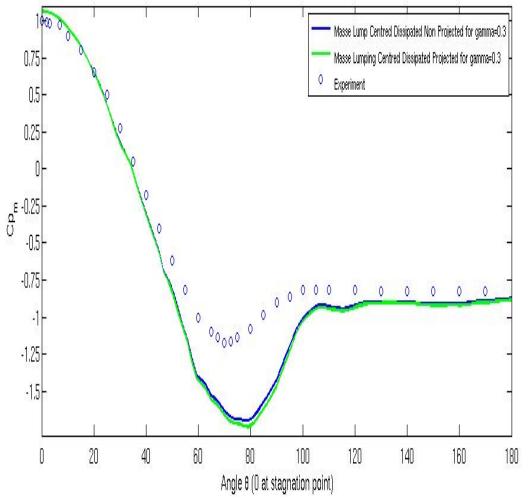

Figure 4.14. Time-averaged and z-averaged pressure distribution on the surface of the cylinder, experiment: Norberg

figure 4.14,for $gamma = 0.3$ we can say the same thing about Mass Lumping Central Diff Proj and NoProj schemes. Between all these schemes, the better results are obtained with Mass Matrix V6 scheme. For all these schemes the pressure coefficient C_p shows discrepancies between 60° and 100°.

Figures (4.15),(4.16),(4.17),(4.18) displays the total resolved Reynolds stress $\overline{u\prime u\prime}$ at $x = 1.54$ and the figures (4.19),(4.20),(4.21),(4.22) displays the total resolved Reynolds stress $\overline{v\prime v\prime}$ at $x = 1.54$.

Here we can observe that the Mass Lumping Central Diff NonProj scheme yields better results than the other ones, for $\gamma = 0.3$.
In the case of total resolved streamwise Reynolds stress $\overline{v\prime v\prime}$ at $x = 1.54$, the best results are obtained with Mass Lumping Central Diff Projected for $\gamma = 0.3$. When we put $\gamma = 1$ we observe that for all the schemes we're getting far away from our experiments.

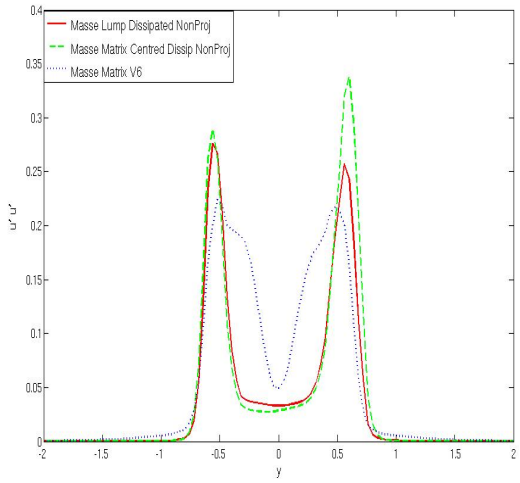

Figure 4.15. Total resolved streamwise Reynolds stress $\overline{u'u'}$ at $x = 1.54$, experiments: Lourenco and Shih (LS)

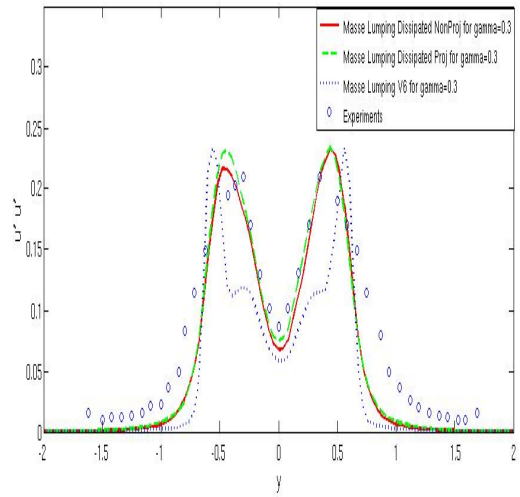

Figure 4.16. Total resolved streamwise Reynolds stress $\overline{u'u'}$ at $x = 1.54$, experiments: Lourenco and Shih (LS)

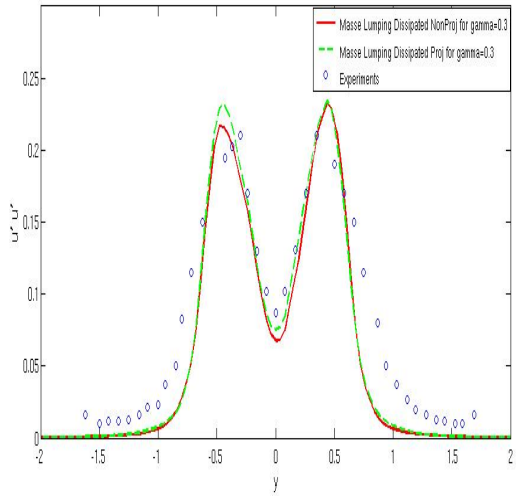

Figure 4.17. Total resolved streamwise Reynolds stress $\overline{u'u'}$ at $x = 1.54$, experiments: Lourenco and Shih (LS)

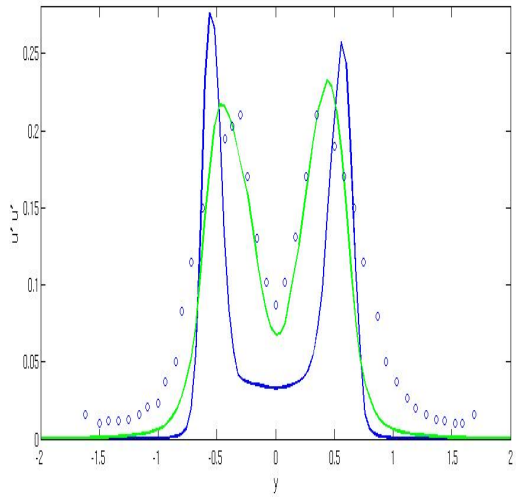

Figure 4.18. Total resolved streamwise Reynolds stress $\overline{u'u'}$ at $x = 1.54$, experiments: Lourenco and Shih (LS)

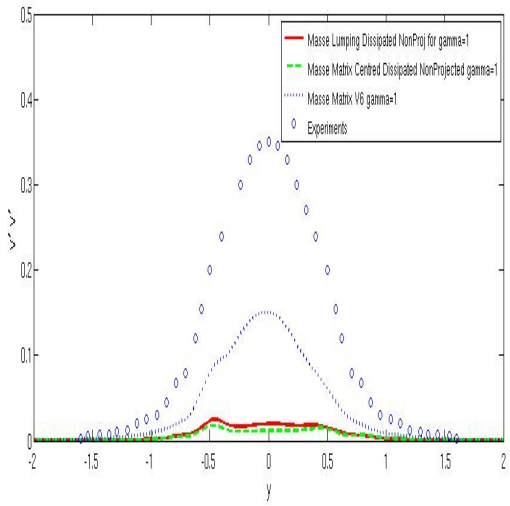

Figure 4.19. Total resolved streamwise Reynolds stress $\overline{v'v'}$ at $x = 1.54$, experiments: Lourenco and Shih (LS)

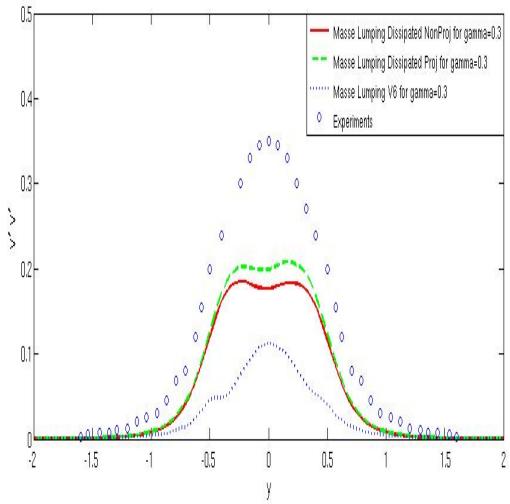

Figure 4.20. Total resolved streamwise Reynolds stress $\overline{v'v'}$ at $x = 1.54$, experiments: Lourenco and Shih (LS)

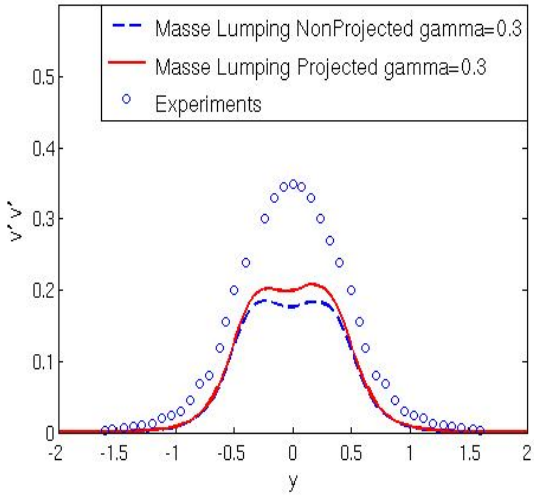

Figure 4.21. Total resolved streamwise Reynolds stress $\overline{v'v'}$ at $x = 1.54$, experiments: Lourenco and Shih (LS)

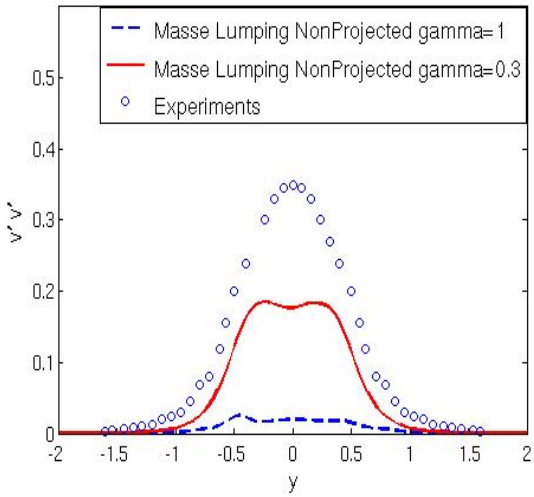

Figure 4.22. Total resolved streamwise Reynolds stress $\overline{v'v'}$ at $x = 1.54$, experiments: Lourenco and Shih (LS)

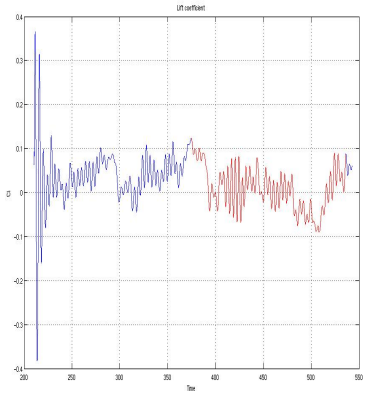

(a)

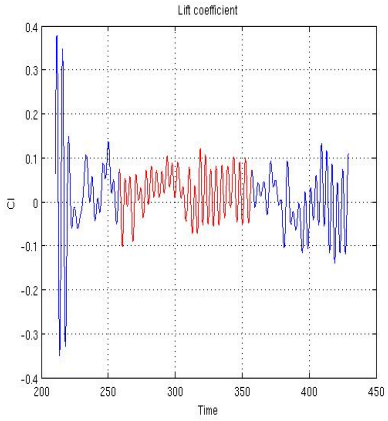

(b)

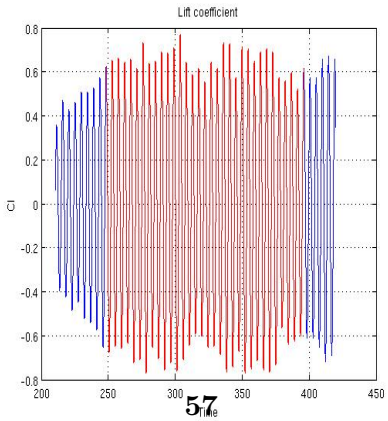

(c)

Figure 4.23. Lift history for Mass Matrix Centeral Diff Non Projected (a) , lift history for Mass Lumping (b) and lift history for Mass Matrix V6 scheme (c) -all these for $\gamma = 1$

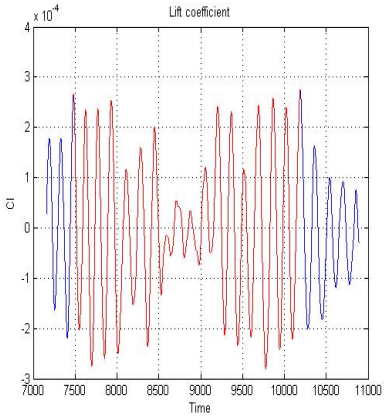

(a)

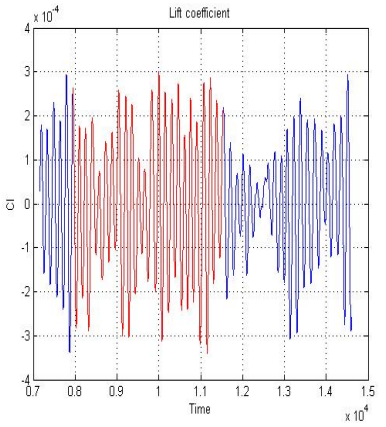

(b)

Figure 4.24. Lift history for Mass Lumping Centeral Diff Non Projected (a) , lift history for Mass Lumping Central Diff Projected(b) -all these for $\gamma = 0.3$

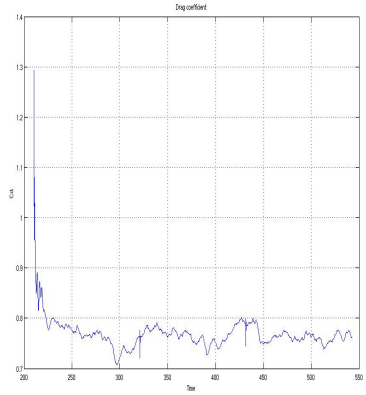

(a)

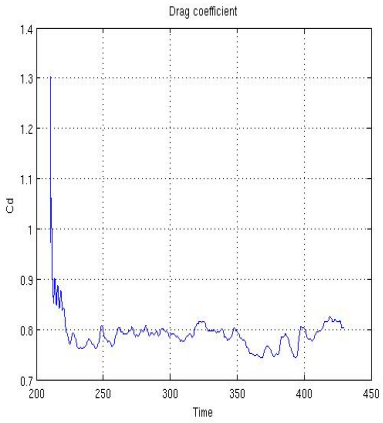

(b)

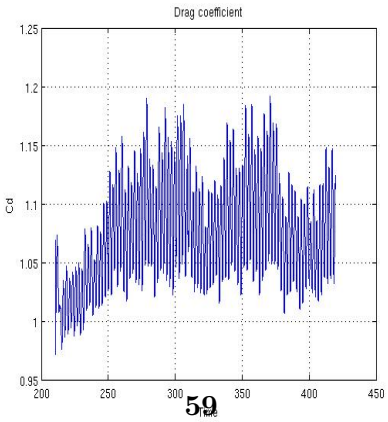

(c)

Figure 4.25. Drag history for Mass Matrix Centeral Diff Non Projected (a) , Drag history for Mass Lumping (b) and drag history for Mass Matrix V6 scheme (c) -all these for $\gamma = 1$

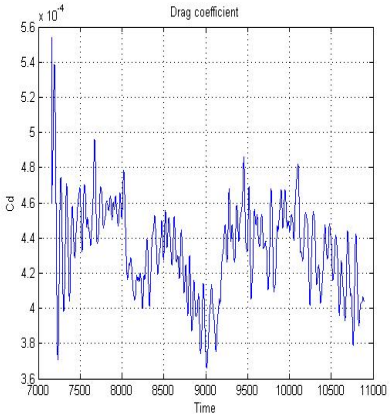

(a)

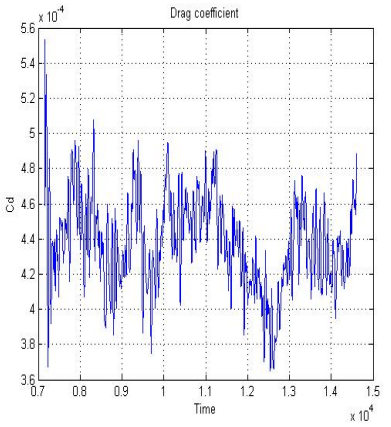

(b)

Figure 4.26. Drag history for Mass Lumping Centeral Diff Non Projected (a) , Drag history for Mass Lumping Central Diff Projected(b) -all these for $\gamma = 0.3$

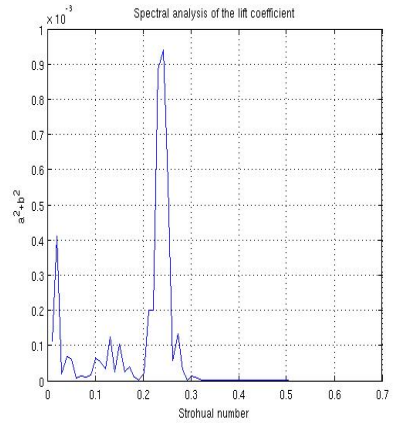

(a)

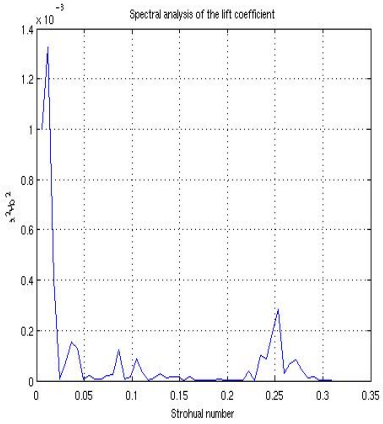

(b)

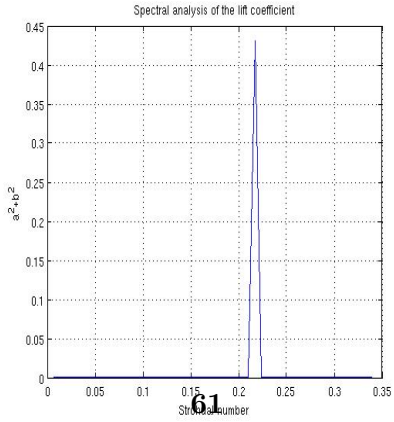

(c)

Figure 4.27. Spectral analysis for Mass Lumping Centeral Diff Non Projected scheme (a) , Spectral analysis for Mass Matrix Central Diff Non Projected scheme (b) and Spectral analysis for Mass Matrix V6 scheme (c) - all these for $\gamma = 1$

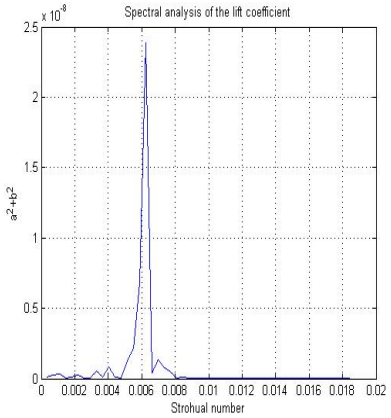

(a)

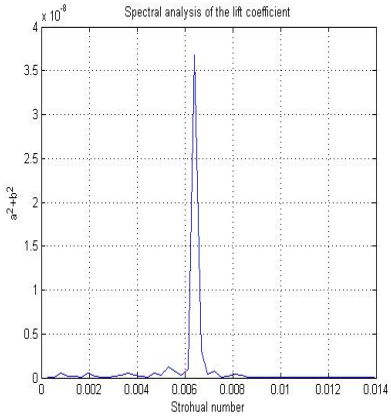

(b)

Figure 4.28. Spectral analysis for Mass Lumping Centeral Diff Non Projected scheme (a) , Spectral analysis for Mass Lumping Central Diff Projected scheme (b) - all these for $\gamma = 0.3$

Chapter 5

Conclusion

We have presented in this work a first investigation of a new Mass Matrix scheme, in order to obtain a better accuracy than for Mass Lumping FV scheme on irregular meshes.

This numerics was installed in a parallel code AERO of research and production. The obtained results for the circular cylinder test are so far less good than those predicted by the Mass Lumping FV scheme with sixth order dissipation which is the basic option for the AERO code.

This Mass Matrix scheme needs to be studied thoroughly before to draw a final conclusion (in particular the implementation and the dissipation term needs to be further investigated).

Bibliography

[1] C. Debiez, *Approximation et linéarisation d"ecoulements aérodynamiques instationnaires*, Ph.D Thesis,Université de Nice Sophia-Antipolis,École doctorale-Sciences pour l'ingénieur,(1996).

[2] C. Farhat, A. Kajasekharan and B. Koobus, *A dynamic variational multiscale method for large eddy simulations on unstructured meshes*, Computational Methods in Applied Mechanics and Engineering, (2005), 1668-1691.

[3] J. Hinze, *Turbulence*, MacGraw-Hill, New York, (1959).

[4] T.J.R. Hughes, L. Mazzei and K.E. Jansen. *Large eddy simulation and the variational multiscale method*, Comput. Vis. Sci., 3, (2000), 47-59.

[5] B. Koobus and C. Farhat, *A variational multiscale method for the large eddy simulation of compressible turbulent flows on unstructured meshes-application to vortex shedding*, Comput. Methods Appl. Mech. Eng., 193, (2004), 1367-1383.

[6] B. Koobus,S. Wornom, S. Camarri, M.-V. Salvetti, A. Dervieux *Nonlinear V6 schemes for compressible flow*, Institut National de Recherche en Informatique et Automatique,30 janvier 2008 (2005), 1668-1691.

[7] G.W. Jones, J.J. Cincotta and R.W. Walker, *Aerodynamic forces on a stationary and oscillating circular cylinder at high Reynolds numbers*, National Aeronautics and Space Administration, NASA TR R-300, (1969).

[8] M.H. Lallemand, H. Steve and A. Dervieux. *Unstructured multigridding by volume agglomeration: current status*, Comput. Fluids, 21, (1992), 397-433.

[9] M.H. Lallemand, *Schemas decentres multigrilles pour la resolution des equations d'Euler en elements finis*, Ph.D Thesis,Université de Provence, Centre Saint Charles, (1988).

[10] C. Norberg, *Effects of Reynolds Number and Low-Intensity Free-Sream Turbulence on the Flow around a Circular Cylinder*, Publ. No. 87/2, Department of Applied Termosc. and Fluid Mech., Chalmer University of Technology, Gothenburg, Sweden, (1987).

[11] L. Ong and J. Wallace, *The velocity field of the turbulent very near wake of a circular cylinder*, Exp. in Fluids, vol.20, Springer Verlag Berlin, (1996) ,441-453.

[12] R. Peyret, *Handbook of computational fluid mechanics*, Academic Press, 2004

[13] P. L. Roe, *Approximate Riemann solvers, parameters, vectors and difference schemes*, J. Comp. Phys., 43, (1981), 357-372.

[14] S. Schmidt and F. Thiele, *Comparison of numerical methods applied to the flow over wall-mounted cubes*, Int. J. of Heat and Fluid Flow, 23, (2002), 330-339.

[15] J. Smagorinsky, *General circulation experiments with the primitive equations*, Monthly Weather Review, 91(3), (1963), 99-164.

[16] P. van Leer, *Towards the ultimate conservative scheme. IV: A new approach to numerical convection*, J. Comp. Phys., 23, (1977), 276-299.

[17] D.C. Wilcox, *Turbulence modeling*, DCW Industries Inc., (1993).

[18] M.M. Zdravkovich, *Flow around circular cylinders*, Oxford University Press, (2003).